XII. PLASMAS AND CONTROLLED NUCLEAR FUSION

A. Active Plasma Systems*

Academic and Research Staff

Prof. L. D. Smullin
Prof. A. Bers
Prof. R. J. Briggs
Prof. R. R. Parker

Graduate Students

R. R. Bartsch
S-L. Chou
J. A. Davis
G. W. Goddard
D. S. Guttman
F. Herba
B. R. Kusse
R. K. Linford
J. A. Mangano
H. M. Schneider

1. ION ENERGY ANALYSIS IN A BEAM-PLASMA DISCHARGE

Previous measurements of electron energies have been made in the beam-plasma discharge (BPD), but no direct measurement has successfully determined the ion energy distribution.[1,2] A study has been made of the various diagnostic techniques for measuring ion energy distributions in the regime 0-100 eV. The retarding potential analyzer was considered the most desirable as a first experiment, because of its simplicity.

A common type of retarding potential analyzer (RPA) consists of a flat plate or a Faraday cup for a collector, and 3 grids. The grid closest to the collector is used to suppress secondary emission, the second grid is used for the variable potential for the ions, and the third grid for repelling the electrons. Electrons can also be analyzed by altering the bias arrangement. Several probes of this general type have been built and tested, and the discovery of various problems ensued. Subsequent modifications have alleviated most of these difficulties.

Figure XII-1 shows the basic construction of the final model. The usual problem of secondary emission from the collector was greatly reduced by using a kind of Faraday cup. A long thin strip of corrugated aluminum foil was wound up like a watch spring and placed in the bottom of the cup; thus, it became statistically more difficult for secondary electrons to find their way out of the cup. The usual techniques of using aquadag coating and a suppressor grid were also employed. In earlier versions of the analyzer, the Debye length of the plasma escaping out of the magnetic mirrors of the BPD was smaller than the mesh size of the grids. As a result, the grids provided no control over the particle current inside the analyzer. The smallest available mesh size (0.2 mm) was used in the construction of the grids, but the Debye length, under certain conditions, was nearly an order of magnitude smaller. In order to increase the Debye length of the

*This work was supported principally by the National Science Foundation (Grant GK-2581).

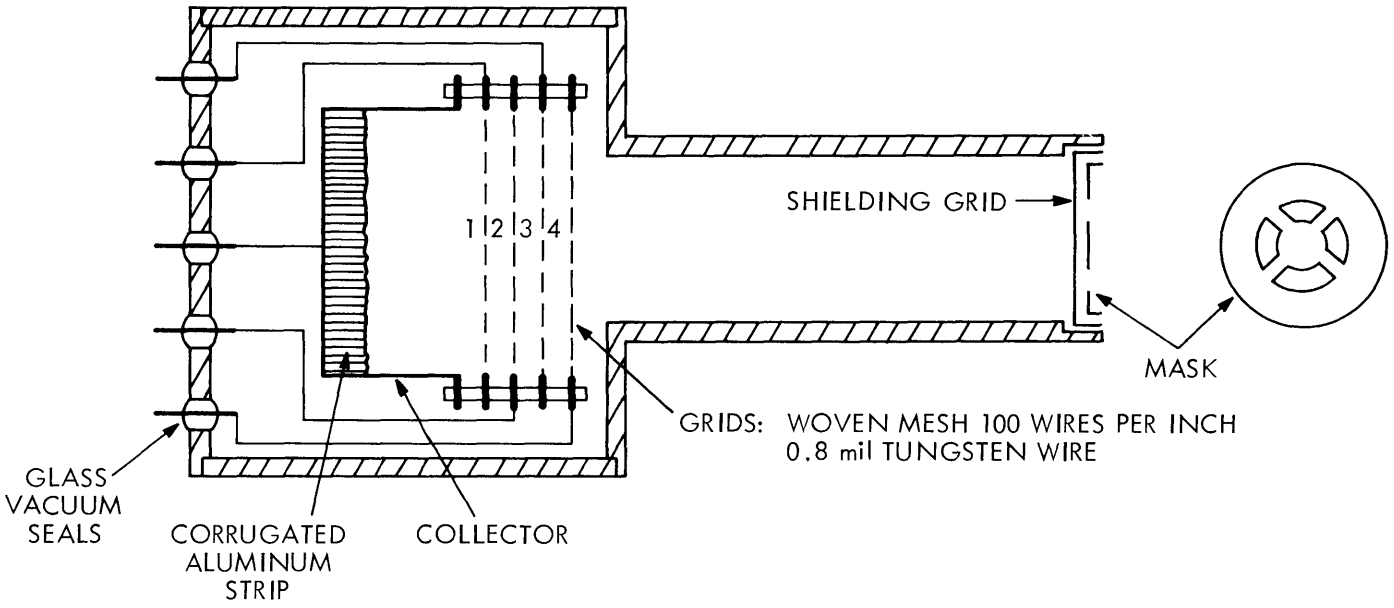

NORMAL BIAS FOR MEASURING ION ENERGY	COLLECTOR	GRID NUMBER			
		1	2	3	4
	-60 V	-180 V	0 V to +40 V	-180 V	-90 V

Fig. XII-1. Final model of the retarding potential analyzer.

plasma entering the analyzer without changing the energy of the constituent particles, the current density was reduced by means of another grid with a smaller mesh size. Since there was ample current (1 A) entering the analyzer, this shielding grid could be quite opaque. A 1.5-mil sheet of copper was photoetched to provide a square array of 100 holes, 0.05 mm in diameter, spaced 1.3 mm apart.

As shown in Fig. XII-1, this grid was placed across the entrance hole of the analyzer and was electrically grounded. Thus the shielding grid successfully repelled all electrons with energies less than the 5-10 V plasma potential found in the BPD.[3] The resulting particle current density was reduced sufficiently to enable the grid biases to control the particle current.

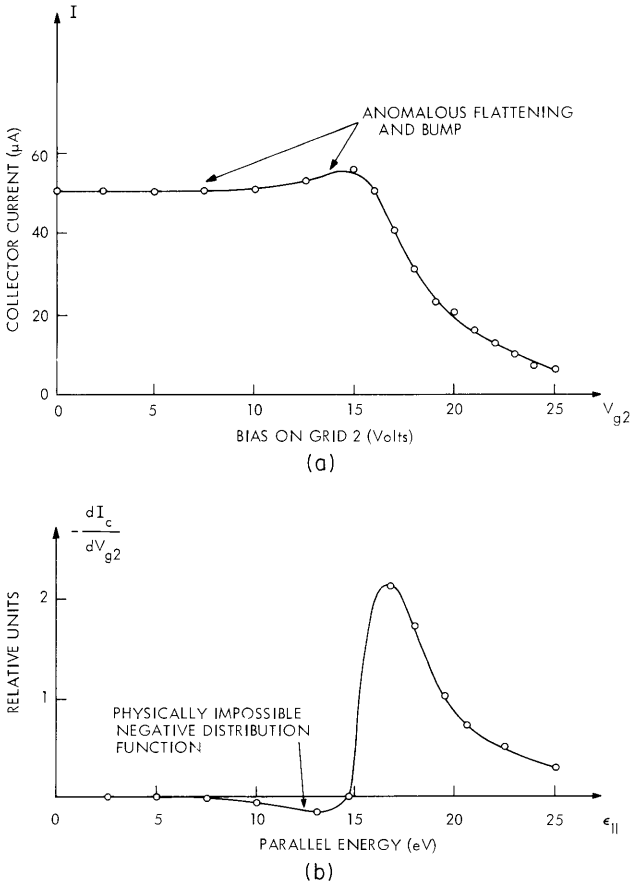

Fig. XII-2. Data obtained from an earlier model of the retarding potential analyzer showing the distortion caused by space-charge limiting.
(a) Collector current vs grid voltage.
(b) Negative derivative of (a), which should be proportional to the parallel energy distribution function.

Some data obtained from earlier models of the RPA exhibited the effects of space-charge limiting. Figure XII-2 points out the anomalous behavior of the collector current arising from space-charge effects. The region in which the "energy distribution function" is negative (Fig. XII-b) is also characterized by enhanced oscillations in the collector current. This phenomena is believed to be due to the instabilities associated with unneutralized ion beams that are beyond critical perveance. This problem was corrected by using the bias arrangement shown in Fig. XII-1 and by the addition of the mask which blocks out 90% of the holes in the shielding grid.

Although the analyzer appears to be functioning properly, another major problem, caused by the turbulence of the plasma of the BPD, remains. Because of the highly structured character of the ion current pulse and its randomlike variation from pulse to pulse, the measurements must be averaged over many pulses to obtain meaningful data. In order to record "instantaneous" profiles, a triangle generator was developed to sweep grid 2 from 0 V to 40 V many times during one beam-current pulse (660 μsec). The block diagram of this generator is shown in Fig. XII-3. The choice of the 3 available frequencies allows one to minimize the laborious averaging of the data for a variety of types

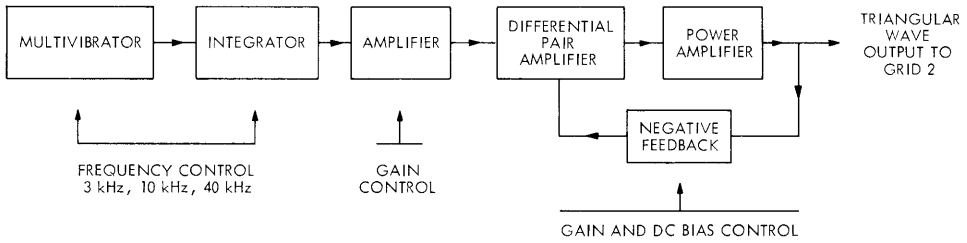

Fig. XII-3. Transistorized triangular wave generator for biasing grid 2.

of structure on the current pulse. The polarity of the triangle wave can also be reversed for measuring electron energies. The generator has a low output impedance, which insures that the voltage will not be appreciably altered because of particle current to the grid. Even though this device greatly eases the task of recording data, some averaging is necessary for highly strucutred current pulses.

Since much of our time has been spent in diagnosing and correcting problems with the analyzer, only preliminary data have been obtained. Despite this, some of the data are at least indicative of what can be expected in the future. Figure XII-4 shows the current versus retarding voltage and the resulting parallel-energy ($V_{||}$) distribution function obtained from the final model of the analyzer. This figure should be compared with Fig. XII-2, which was obtained before the space-charge corrections were made. The energy distribution in Fig. XII-4b is not Maxwellian and has an average energy of approximately 9 eV. Both the shape of the distribution function and the average energy

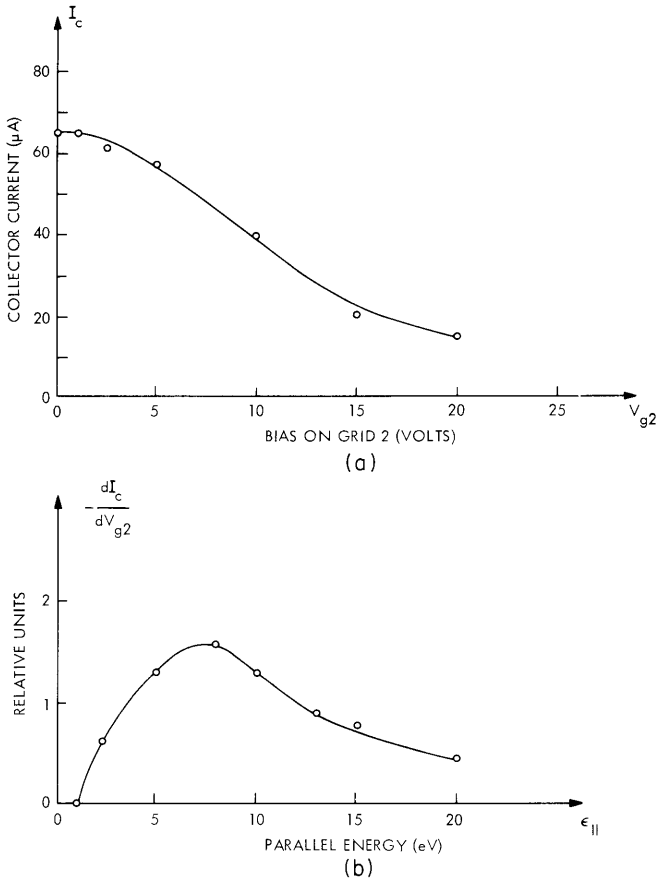

Fig. XII-4. Data obtained from the final model of the retarding potential analyzer with the following parameters: triangular wave period, 100 μsec, 200 μsec after the beginning of the beam pulse; beam voltage, 12 kV, beam current, 11 A; gas pressure, 7×10^{-4} Torr; magnetic field at the mirror peak, 50 kG, with a mirror ratio of 3.
(a) Collector current vs grid voltage.
(b) Ion parallel energy distribution.

are observed to be strong functions of time, gas pressure, and beam power. Average parallel energies ranging from 3 eV to 12 eV have been measured.

It is difficult to say much about the velocity distribution of ions inside the magnetic mirrors, since we know only the parallel velocity distribution of the escaping ions. A knowledge of the total energy distribution of the escaping ions would help greatly. This can be measured by allowing the ions to drift out of the magnetic mirror along the axis to a point where the magnetic field becomes small in comparison to the field at the mirror peak. At this point most of the perpendicular energy of the ions has been transferred to the parallel direction so that the total energy of the particle can be measured. This is

presently being tried and preliminary measurements indicate total average ion energies near 20 eV.

In the immediate future a series of measurements will be taken of the total energy distribution and the parallel energy distribution as a function of beam power, magnetic field, and gas pressure. This will be done with continuous gas flow. It is hoped that a theory will be developed relating these quantities to the velocity distribution function of the ions trapped in the magnetic mirrors. We have not yet succeeded in making similar measurements with the pulsed-gas beam-plasma discharge. Since the analyzer and the gas valve are both connected to the beam collector, the gas burst overloads the analyzer.

R. K. Linford, L. D. Smullin

References

1. R. R. Bartsch, Quarterly Progress Report No. 85, Research Laboratory of Electronics, M.I.T., April 15, 1967, pp. 146-149.
2. R. R. Bartsch, Quarterly Progress Report No. 86, Research Laboratory of Electronics, M.I.T., July 15, 1967, pp. 143-147.
3. R. R. Parker, Ph.D. Thesis, Department of Electrical Engineering, M.I.T., 1967, p. 78 (unpublished).

2. MINIMUM-B MIRROR MAGNETIC FIELD IN SYSTEM A

The minimum-B field is produced by discharging a 60-μF capacitor bank through a hexapole geometrical configuration,[1] crowbarring the hexapole by means of an ignitron when the current is at maximum.

The problem of crowbarring has been solved by (a) using a parallel plate transmission line from the capacitor bank to the hexapole, and (b) placing the crowbarring ignitron as close as possible to the input terminals of the hexapole (this also provides for transferring most of the electric energy to the hexapole field). The arrangement is shown in Fig. XII-5. The inductance associated with the hexapole is of the order of 1 μH. It was then necessary to minimize the inductance associated with the leads. By making the plate separation small (1/8") and the width of the plates large (7"), the inductance of the line was minimized (to approximately 2.5 nH). In order to minimize the inductance associated with the crowbarring ignitron's header, the outer electrode was coaxially mounted as shown. (As for the intrinsic inductance of the ignitron, there is not much that one can do.) Pulse transformers with 1:1 secondary provide the triggering for the ignitrons with a 1-kV thyratron pulse. Both thyratrons are triggered simultaneously. For the crowbarring ignitron, the rise time of its triggering pulse is such as to provide a delay of approximately 18 μsec with respect to the switching ignitron. At this

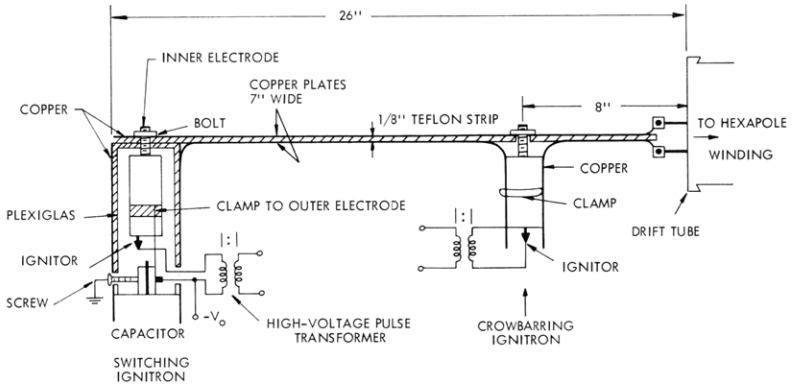

Fig. XII-5.
Circuit for excitation of the hexapole winding.

time, crowbarring occurs with the current just past its maximum value.

The hexapole field is monitored by a 5-turn coil, $1\frac{3}{4}$" in diameter. The coil is placed on the outside with its axis parallel to one of the hexapole conductors. By passing the output of the coil through an integrator, the current waveform is obtained. Figure XII-6 is an oscillograph of this current for a voltage of 1 kV in the capacitor

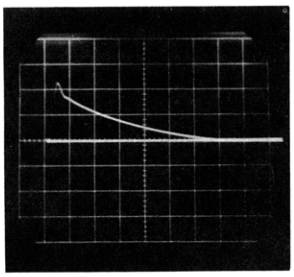

Fig. XII-6. Current through hexapole winding. Capacitor bank voltage: 1 kV. Vertical axis: 1 V/cm. Horizontal axis: 50 μsec/cm.

bank. A calibration of the coil yields 0.32 mV/A. Thus, from Fig. XII-6, it is seen that 1 kV results in a peak current of 6.7 kA. If we now assume that all of the electric energy is changed into magnetic energy, we have

$$\frac{1}{2} C V_o^2 = \frac{1}{2} L I_{peak}^2,$$

where C = 60 μF, L = 1 μH, V_o = 1 kV. Thus $I_{peak} \approx 7.7$ kA. The discrepancy is mainly due to the fact that the actual inductance, because of leads and the crowbarring ignitron by itself, is somewhat higher than 1 μH. With this in mind, the measured value of the current is quite reasonable. After crowbarring we are left with an equivalent R-L circuit. From Fig. XII-6, the time constant is approximately 120 μsec, and for L ≈ 1 μH the resistance of the hexapole plus ignitron is then approximately 8 mΩ.

Preliminary Observations

For the beam-plasma discharge, hydrogen gas was fed continuously into the system through a needle valve.[1]

With a pressure of $\sim 2 \times 10^{-4}$ mm Hg and a beam voltage of 10 kV, a 300-kHz oscillation was detected by means of a photomultiplier placed perpendicular to the axis of the drift tube. This frequency is close to that observed by Hartenbaum,[2] corresponding to a rotating vane of plasma. With the pressure and the beam voltage fixed, the oscillation only occurred for a field strength of approximately 200 G at the center of the mirror (mirror ratio ≈ 3.5). By pulsing the hexapole field simultaneously with the beam and the capacitor bank at 1 kV, the oscillation was suppressed. We also noticed that the light signal would decrease, thereby indicating that the plasma column might be displaced. Also, it is not clear, at present, whether or not the radius of the column is being decreased by the minimum-B field.

F. Herba, R. R. Parker

References

1. F. Herba and J. G. Siambis, Quarterly Progress Report No. 85, Research Laboratory of Electronics, M.I.T., April 15, 1967, pp. 154-156.
2. B. Hartenbaum, "Experimental Investigation of the Beam-Plasma Discharge," Ph.D. Thesis, Department of Mechanical Engineering, M.I.T., May 1964.

3. BEAM-PLASMA DISCHARGE: SYSTEM D

The periodic field monotron model proposed for the experimental observations of a low-frequency beam-plasma interaction with a low-level beam in the afterglow plasma of System D[1] has been applied to the experimental results of Lieberman.[2] The monotron treatment of Wesselberg has been adapted to the field pattern of the plasma cavity oscillations.[3] The Landau damping of the plasma-cavity oscillations by the hot electrons has been determined for the parabolic mirror system of finite length by adapting the treatment of infinite system Landau damping which is due to Stix.[4]

Monotron Model for Lieberman's Experimental Results

Lieberman observed an interaction between a 300-V beam and the afterglow plasma of an electron-cyclotron resonance discharge. The electron density decay measured by Lieberman is shown in Fig. XII-7. The interaction, observed as a modulation on the beam collector current, occured during relaxation oscillation in which cold electrons were driven from the system. Lieberman did not, however, measure the cold electron density during the relaxation oscillation. We have calculated frequency shifts for

Lieberman's experimental conditions from the resonant plasma-cavity solutions previously described by assuming ratios of cold-to-hot electron density during the

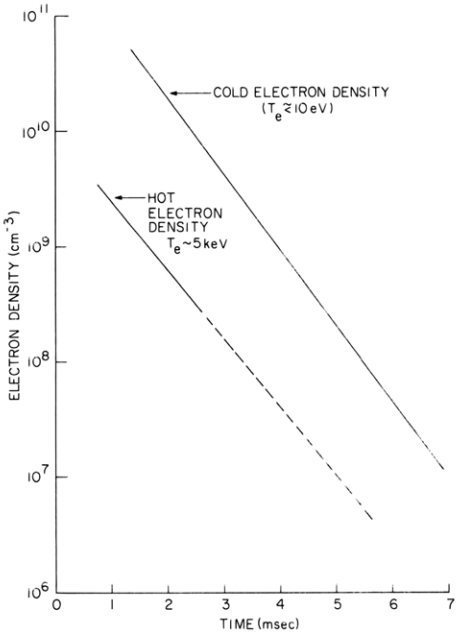

Fig. XII-7. Experimental density decay for Lieberman ECRD experiment.

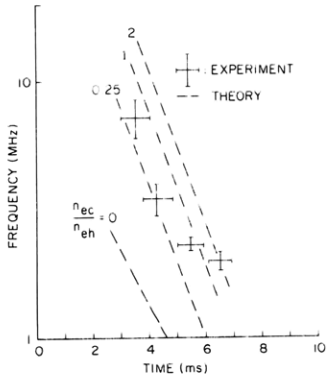

Fig. XII-8. Theoretical and experimental frequencies for an electron beam in ECRD afterglow.

relaxation oscillation.[5] These shifts are shown in Fig. XII-8, together with the observed oscillation frequency at various times in the afterglow, where the interaction frequency has been determined by the condition $k = \pi/L$. We have

$$f = \sqrt{\frac{p^2 f_{pi}^2 + k^2 f_{pe\ cold}^2}{p^2 + k^2 + \omega_{pe\ hot}^2/v_T^2}}.$$

Cold-to-hot electron density ratios in the range 0.25-2 agree with Lieberman's experimental frequency shift.

Negative-Conductance Monotron Model

Wesselberg has treated the general case of an electron beam in a standing slow wave. The current density in the beam is related to the electric field of the slow-wave structure by the following expression[6]:

$$\frac{\partial^2 J}{\partial z^2} + 2jke\frac{\partial J}{\partial z} + \left(k_p^2 - k_e^2\right)J = j\omega\epsilon_o k_p^2 E(z),$$

where the beam is assumed to be immersed in an infinite z-directed magnetic field, and E and J vary as $e^{j\omega t}$, k_e is the electronic wave number, ω/v_o, and k_p is the beam-plasma wave number, $\omega_{p\ beam}/v_o$. The solution of the expression above for an electric field of the form

$$E_o \sin \pi z/L \qquad \left(-\frac{L}{2} \leq z \leq \frac{L}{2}\right)$$

has been determined. The power flow from the slow-wave circuit to the beam is given by

$$P = k_p \frac{\omega\epsilon_o}{4} |E_o|^2 \left\{ \frac{\cos^2\left[(k_e - k_p)\frac{L}{2}\right](k_e - k_p)^2}{\left[(k_e - k_p)^2 - \left(\frac{\pi}{L}\right)^2\right]^2} - \frac{\cos^2\left[(k_e + k_p)\frac{L}{2}\right](k_e + k_p)^2}{\left[(k_e + k_p)^2 - \left(\frac{\pi}{L}\right)^2\right]^2} \right\}.$$

The beam can give up energy to the standing-wave pattern over certain ranges of the frequency and space-charge parameters. The conductance that the beam presents

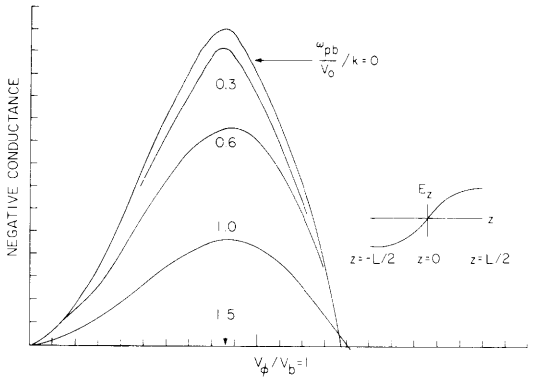

Fig. XII-9. Small-signal conductance for the $\lambda/2$ system.

to the slow-wave resonator is negative in these ranges. The normalized, low-frequency, small-signal beam conductance,

$$g_e \sim \frac{P}{|E_o|^2},$$

is shown in Fig. XII-9 as a function of $v_\phi/v_b = \omega L/\pi v_o$, with the beam space charge as a parameter. The beam conductance is observed to be negative in the range of parameters $\omega \leq 1.4\ \pi v_o/L$ and $\omega_p \leq 1.5\ \pi v_o/L$.

Landau Damping and a Parabolic Mirror System

Stix has given a derivation of Landau damping in an infinite, one-dimensional system, wherein the damping rate of a traveling wave with electric field,

$$\vec{E} = \dot{T}_z E_o \cos(kz-\omega t),$$

is found by integrating the force equation for a particle at a velocity v_o with a perturbation solution

$$z = z_o(t) + z_1(t) + z_2(t) + \ldots,$$

where $z_o(t)$ is the unperturbed particle motion, $v_o(t) + z\ (t = 0)$. The rate of change of particle energy is averaged over the initial position of the electron with respect to the wave and over the electron distribution function to find the damping rate. We have modified this procedure by adding to the force equation the confining force attributable to a parabolic mirror and considering the damping of a standing-wave pattern. The undriven axial particle motion in a parabolic magnetic mirror is described by solutions of

$$\frac{d^2z}{dt^2} + \omega_m^2 z = 0,$$

where ω_m is the particle mirror transit frequency (the particle perpendicular velocity) at the midplane divided by the range of the parabolic mirror). We have the driven force equation of the particles in a standing wave $E_o \sin kz \sin \omega t$ given by

$$\frac{d^2z}{dt^2} + \omega_m^2 z = \frac{eE_o}{m} \sin kz \sin(\omega t+\psi).$$

This equation has been solved for the case in which particles do not venture very far out from z = 0: kz < 1. The time variation of the particle energy is given by

$$\Delta E = \frac{mv_{\parallel}^2}{16\tau^4}\left[\frac{2\sin^2\left(\frac{v_\perp}{a}-\frac{\omega}{2}\right)t}{\omega\frac{v_\perp}{a}\left(\frac{v_\perp}{a}-\frac{\omega}{2}\right)^2} - \frac{2\sin^2\left(\frac{v_\perp}{a}+\frac{\omega}{2}\right)t}{\omega\frac{v_\perp}{a}\left(\frac{v_\perp}{a}+\frac{\omega}{2}\right)^2} + \frac{\sin\left(\frac{v_\perp}{a}-\frac{\omega}{2}\right)t\,\sin\left(\frac{v_\perp}{a}+\frac{\omega}{2}\right)t}{\omega^2\left(\frac{v_\perp}{a}-\frac{\omega}{2}\right)\left(\frac{v_\perp}{a}+\frac{\omega}{2}\right)}\right]$$

for a particle with midplane velocities $v_{\parallel}$ and $v_\perp$ in a magnetic field described by $B(z) = B_o\left(1+\left(\frac{z}{a}\right)^2\right)$. Here, τ is the trapping time in the usual treatment of Landau damping, $\sqrt{m/eE_o k}$. Integrating over the mirror midplane distribution function

$$f \sim e^{-mv_\perp^2/2k\tau_\perp} e^{-mv_\parallel^2/2k\tau_\parallel} \qquad v_\parallel < \sqrt{R-1}\, v_\perp,$$

where R is the mirror ratio, and $\tau_\perp$ and $\tau_\parallel$ are the perpendicular and parallel midplane electron temperatures, we find that the energy change in the system is given by

$$\overline{\Delta E} = t\frac{\omega_p^2}{\omega} V \frac{\left[\sqrt{R-1}\,(\omega a/2)\right]^3}{\left(\frac{2\pi k\tau_\perp}{m}\right)\left(\frac{2\pi k\tau_\perp}{m}\right)^{1/2}} \frac{(ka)^2}{6} \epsilon_o E_o^2 \pi^2 e^{-m/2k\tau_\perp (\omega a/2)^2}$$

for standing wave-frequencies such that $\left[\sqrt{R-1}\,(\omega a/2)\right]^2 \lesssim 0.5(2k\tau_\parallel/m)$. V is the volume of the system. The particle energy is observed to grow linearly with time at a rate determined by the number of electrons in synchronism with the standing-wave pattern ($v_\perp$ synchronism $= \omega a/2$).

The effects of an axial density variation on the plasma-cavity resonances and the generalization of the finite-length-system Landau-damping model are now being investigated.

R. R. Bartsch

References

1. R. R. Bartsch, "Beam-Plasma Discharge: System D," Quarterly Progress Report No. 88, Research Laboratory of Electronics, M.I.T., January 15, 1968, pp. 170-173.
2. M. A. Lieberman, "Ion Oscillations Excited by Electron Beam-Plasma Interaction," Ph.D. Thesis, Department of Electrical Engineering, M.I.T., June 1966.
3. T. Wesselberg, "A General Theory of Klystrons with Arbitrary Extended Interaction Fields," Report NO1 376, Microwave Laboratory, Stanford University, March 1957.
4. T. H. Stix, The Theory of Plasma Waves (McGraw-Hill Publishing Company, New York, 1962), Sec. 7-2.
5. R. R. Bartsch, op. cit., p. 172
6. T. Wesselberg, op. cit.; see Eq. 9-17.

4. OSCILLATIONS IN AN INHOMOGENEOUS COLD PLASMA

Some interesting results have recently been obtained for the asymptotic response of an inhomogeneous cold plasma to an intitial density or velocity perturbation.[1] For a plasma column having a smooth density profile with a maximum in the center, the results are particularly simple when there is no applied DC magnetic field. In this case the external fields for long times are damped sinusoids, with a damping rate proportional to $\frac{1}{t^n}$. The "ringing" frequency of the sinusoid is the plasma frequency at the center of the column.

In this report we present a derivation of the complete time dependence of the voltage across a one-dimensional inhomogeneous plasma and evaluate it for a specific density profile. The results agree asymptotically with those of Baldwin, Henderson, and Hirshfield.[1]

Consider a cold, one-dimensional plasma in which ions and electrons have the density distribution $n_o(x)$ in the unperturbed state. We assume that the ions have an infinite mass and act only as a neutralizing background with the density $n_o(x)$. If a perturbation in the electron density or velocity is made at $t = 0$, we wish to find the electron density $n_e(x,t)$, the electric field $E(x,t)$ and the velocity $v(x,t)$ for $t > 0$. The linearized fluid equations are

$$\frac{\partial n_1}{\partial t} = -\frac{\partial}{\partial x}(n_o x) \tag{1}$$

$$\frac{\partial v}{\partial t} = -\frac{e}{m}E \tag{2}$$

$$\frac{\partial E}{\partial x} = -\frac{e}{\epsilon_o}n_1, \tag{3}$$

where $n_e(x,t) = n_o(x) + n_1(x,t)$. The mass of an electron is m, and the magnitude of its charge is e. Laplace-transforming these equations in time, we obtain

$$s\tilde{n}_1 - n_1(x,O) + \frac{d}{dx}(n_o\tilde{v}) = 0 \tag{4}$$

$$s\tilde{v} - v(x,O) = -\frac{e}{m}\tilde{E} \tag{5}$$

$$\frac{d\tilde{E}}{dx} = -\frac{e}{\epsilon_o}\tilde{n}_1, \tag{6}$$

where, for example, $n_1(x,t) = \frac{1}{2\pi j}\int_{-j\infty+\sigma}^{+j\infty+\sigma}\tilde{n}_1(x,s)\,e^{st}\,ds$. Solving for the transform of the electric field, we find

$$\tilde{E}(x,s) = \frac{-\frac{se}{\epsilon_o}\int_{-\infty}^{x} n_1(x',O)\,dx' + \frac{e}{\epsilon_o} n_o(x)\, v(x,O)}{s^2 + \omega_p^2(x)}, \tag{7}$$

where $\omega_p^2(x) = \frac{e^2 n_o(x)}{\epsilon_o m}$. From Eq. 7 we can find the electric field as a function of time.

$$E(x,t) = \left[-\frac{e}{\epsilon_o}\int_{-\infty}^{x} n_1(x',O)\,dx'\right]\cos\left[\omega_p(x)t\right] + \frac{m\epsilon_o\omega_p(x)\, v(x,O)}{e}\sin\left[\omega_p(x)t\right]. \tag{8}$$

The voltage appearing across the plasma is

$$V(t) = -\int_{-\infty}^{+\infty}\frac{1}{2\pi j}\int_{-j\infty+\sigma}^{+j\infty+\sigma} E(x,s)\, e^{st}\, ds\,dx. \tag{9}$$

For the special case of a plasma that has $n_o(x) = \frac{n_c}{1+x^2}$, where n_c is the plasma density in the center ($x = 0$), we can obtain a simple expression for the voltage. Suppose all of the particles are given a small displacement δ at $t = 0$. Then $n_1(x,O) = -\delta\frac{dn_o}{dx}$ and Eq. 8 yields

$$E(x,t) = \frac{e\delta}{\epsilon_o} n_o(x)\cos\left[\omega_p(x)t\right]. \tag{10}$$

The voltage is given by

$$V(t) = -\frac{e\delta n_c}{\epsilon_o}\int_{-\infty}^{+\infty}\frac{1}{1+x^2}\cos\left(\frac{\omega_{pc}}{\sqrt{1+x^2}}t\right)dx, \tag{11}$$

where $\omega_{pc} = \left(\frac{e^2 n_c}{\epsilon_o m}\right)^{1/2}$ is the plasma frequency at $x = 0$. By using the substitution $\cos\theta = \frac{1}{\sqrt{1+x^2}}$, Eq. 11 becomes

$$V(t) = -\frac{2e\delta n_c}{\epsilon_o}\int_0^{\pi/2}\cos\left(\omega_{pc}t\cos\theta\right)d\theta \tag{12}$$

or

$$V(t) = -\frac{e\delta n_c \pi}{\epsilon_o} J_o(\omega_{pc}t). \tag{13}$$

For the density $n_o(x)$ considered above we can also find the expression for $V(t)$ from

Eq. 9 by integrating first over x. We must calculate

$$\tilde{V}(s) = -\int_{-\infty}^{+\infty} E(x, s)\, dx \tag{14}$$

which yields

$$\tilde{V}(s) = -\int_{-\infty}^{+\infty} \frac{\frac{se\delta n_o(x)}{\epsilon_o}\, dx}{s^2 + \frac{e^2 n_o(x)}{\epsilon_o m}}. \tag{15}$$

For $n_o(x) = \frac{n_c}{1 + x^2}$ this becomes

$$\tilde{V}(s) = -\frac{se\delta n_c}{\epsilon_o} \int_{-\infty}^{+\infty} \frac{dx}{s^2x^2 + \left(s^2 + \omega_{pc}^2\right)}. \tag{16}$$

The integral in Eq. 16 is along the real x axis and may be evaluated by residues to yield for V(s)

$$\tilde{V}(s) = -\frac{en_c\delta}{\epsilon_o} \frac{\pi}{\sqrt{s^2 + \omega_{pc}^2}}. \tag{17}$$

Inverse-transforming (17), we again obtain

$$V(t) = -\frac{en_c\delta\pi}{\epsilon_o} J_o(\omega_{pc}t). \tag{18}$$

This result is in agreement with that of Baldwin, Henderson, and Hirshfield, in that asymptotically in time Eqs. 13 and 18 give

$$V(t) \approx -\frac{en_c\delta\pi}{\epsilon_o} \sqrt{\frac{2}{\pi\omega_{pc}t}} \cos\left(\omega_{pc}t - \frac{\pi}{4}\right). \tag{19}$$

In order to show the transition from an inhomogeneous plasma to a uniform plasma of finite extent, consider the equilibrium density

$$n_o(x) = \frac{n_c}{1 + x^{2n}} \qquad n = 1, 2, \ldots . \tag{20}$$

For a uniform displacement perturbation of amplitude δ, the Laplace transform of the voltage (Eq. 15) becomes

$$\tilde{V}(s) = -\frac{en_c\delta}{\epsilon_o}\frac{\pi}{n\sin\frac{\pi}{2n}}\left[s^{\left(1-\frac{1}{n}\right)}\left(s^2+\omega_{pc}^2\right)^{\left(\frac{1}{2n}-1\right)}\right]. \tag{21}$$

If $n = 1$ in Eq. 20, we recover the density distribution discussed above, and $V(s)$ in Eq. 21 agrees with Eq. 17. For $n \to \infty$, the density function in Eq. 20 approaches a uniform plasma of density n_c extending from $x = -1$ to $x = +1$, and the Laplace-transformed voltage is

$$\tilde{V}(s)\Big|_{n\to\infty} = -\frac{2en_c\delta}{\epsilon_o}\frac{s}{s^2+\omega_{pc}^2}, \tag{22}$$

which gives a time-dependent voltage

$$V(t) = -\frac{2en_c\delta}{\epsilon_o}\cos\omega_{pc}t. \tag{23}$$

Thus, as the plasma becomes uniform, the voltage oscillation is no longer damped, in agreement with the simple linear theory model for plasma slab oscillations.

A. Bers, H. M. Schneider

References

1. D. E. Baldwin, D. M. Henderson, and J. L. Hirshfield, Phys. Rev. Letters 20, 7 (12 February 1968).

5. COMPUTER SIMULATION OF AN INHOMOGENEOUS PLASMA

Previously, we have described the computer simulation of a one-dimensional inhomogeneous plasma with ion and electron charge sheets.[1] The ion sheets represented a stationary neutralizing background and only the dynamics of the electron sheets were studied. An alternative approach is to represent the ion background as a continuous density distribution, and use charge sheets only for the electrons. This model has been employed by Dawson[2] and others for an infinite, uniform plasma.

In simulating a nonuniform plasma with this technique some important differences arise, the details of which will be given here.

As an example, we shall describe the computer simulation of an inhomogeneous cold plasma in which ions and electrons have the equilibrium density $n_o(x) = \frac{n_c}{1 + x^2}$. The dynamics of electron charge sheets moving through the stationary ion background with density $n_o(x)$ are to be found. In equilibrium, a number of electron sheets N_s is distributed in such a way that the average electric field acting on each sheet is zero. If the electron sheets all have the same charge per unit area, σ, the constraint that the entire plasma be neutral gives

$$N_s\sigma = -e\int_{-\infty}^{+\infty} \frac{n_c}{1 + x^2}\,dx, \tag{1}$$

where e is the magnitude of the charge on an electron. Thus the charge per unit area on an electron sheet is

$$\sigma = \frac{-e\pi n_c}{N_s}. \tag{2}$$

We now consider the problem of placing these N_s electron sheets in their equilibrium positions. Assume that the first electron sheet is to be placed at $x = x_{o1}$ and that there are no electron sheets with equilibrium positions less than x_{o1}. The constraint that the average field on this sheet be zero gives

$$-e\int_{-\infty}^{x_{o1}} \frac{n_c\,dx}{1 + x^2} = \frac{\sigma}{2} = -\frac{e\pi n_c}{2N_s} \tag{3}$$

or

$$x_{o1} = \tan\left[+\frac{\pi}{2}\left(-1 + \frac{1}{N_s}\right)\right]. \tag{4}$$

If the other sheets are given equilibrium positions in sequence after this one the k^{th} sheet would be placed at

$$x_{ok} = \tan\left[\frac{\pi}{2}\left(-1 + \frac{2k-1}{N_s}\right)\right] \qquad (5)$$

$$k = 1, \ldots\ldots, N_s.$$

A sketch of the electric field across the plasma in equilibrium is shown in Fig. XII-10, where it has been assumed that $N_s = 5$ for the purpose of illustration. Note that there is a field between the sheets, but that the average field acting on each one is zero.

The dynamics of the electron sheets is found by solving the equation of motion for each sheet. This equation is

$$\frac{d^2x_k}{dt^2} = -\frac{e}{m}E_k, \qquad (6)$$

where e/m is the charge-to-mass ratio of an electron, x_k is the instantaneous position of the k^{th} sheet, and E_k is the average electric field acting in the k^{th} sheet.

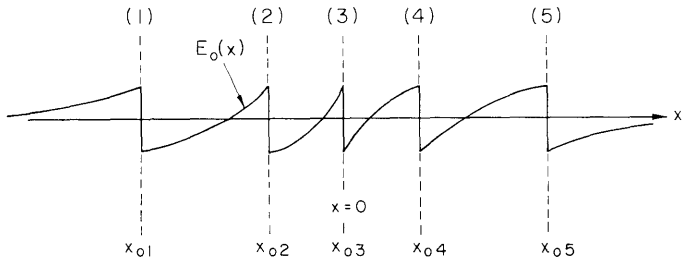

Fig. XII-10. Electric field as a function of distance in an inhomogeneous plasma modeled by five electron sheets and a continuous ion density.

In the absence of any electron sheet crossings, this electric field is given by

$$E_k = \frac{e}{\epsilon_o}\int_{x_{ok}}^{x_k} \frac{n_c dx}{1+x^2}, \qquad (7)$$

so that the equation of motion becomes

$$\frac{d^2x_k}{dt^2} = -\omega_{pc}^2\left[\tan^{-1}x_k - \tan^{-1}x_{ok}\right], \qquad (8)$$

where ω_{pc} is the plasma frequency in the center of the ion distribution. If two electron sheets cross, the equation of motion is corrected by interchanging the equilibrium positions of the two sheets.[2] The important difference between our result (8) and that obtained for a uniform plasma is that the equation of motion for each electron sheet is

nonlinear in x_k for the inhomogeneous plasma.

In order to check this computer model, the equations of motion (8) have been integrated by a Runge-Kutta method for an initial displacement perturbation that has the initial conditions $\frac{dx_k}{dt} = 0$ and $x_k = x_{ok} + \delta$. The number of sheets used was 1000, and $\delta = 0.1$. As is shown in another report,[3] the voltage across the plasma for small initial displacements should be $V(t) = -\frac{\delta e \pi n_c}{\epsilon_o} J_o(\omega_{pc} t)$. The voltage as obtained in the computer experiment, as well as the theoretical result, is given in Fig. XII-11. As can be seen,

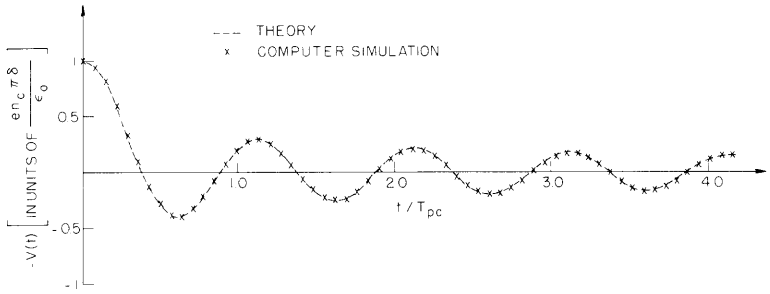

Fig. XII-11. Voltage across an inhomogeneous plasma with density $n(x) = \frac{n_c}{1 + x^2}$ for an initial displacement perturbation ($\delta = 0.1$).

there is very good agreement between the two. The voltage has been plotted only to the time at which two electron sheets first cross, which is $t/T_{pc} \approx 4.16$ experimentally. The time of first crossing was derived analytically in a previous report[4] and found to be

$$t_o \approx \frac{1}{|\delta\omega_p'|} \tag{9}$$

for small displacements δ. In Eq. 9, ω_p' is $\frac{d\omega_p(x)}{dx}$ evaluated where $\frac{d^2\omega_p(x)}{dx^2} = 0$. For the density distribution that was used,

$$\omega_p(x) = \frac{\omega_{pc}}{\sqrt{1 + x^2}}, \tag{10}$$

which has $\frac{d^2\omega_p}{dx^2} = 0$ at $x = \pm\frac{1}{\sqrt{2}}$. At this value of x, $|\omega_p'| = 2\omega_{pc}/3\sqrt{3}$, so that $\omega_{pc} t = 3\sqrt{3}/2\delta = 26$ for $\delta = 0.1$. Hence, $t_o/T_{pc} = 4.14$, which is in good agreement with the computer experimental results.

The computer simulation is being continued in order to determine the effects of crossings on the damping of the oscillations. The damping resulting from thermal motion of the electrons in an inhomogeneous plasma will also be investigated.

H. M. Schneider

References

1. H. M. Schneider, Quarterly Progress Report No. 87, Research Laboratory of Electronics, M.I.T., October 15, 1967, p. 112.
2. J. M. Dawson, Phys. Fluids 5, 445 (1962).
3. H. M. Schneider, see Sec. XII-A.4.
4. H. M. Schneider, Quarterly Progress Report No. 86, Research Laboratory of Electronics, M.I.T., July 15, 1967, p. 163.

6. FURTHER DISCUSSION ON ELECTRON BEAM SPACE-CHARGE WAVE INTERACTION WITH THE BACKWARD WAVE IN A COLD-PLASMA WAVEGUIDE

We have previously reported[1] on the absolute instability arising from beam space-charge wave interaction with the backward plasma wave in a cold-plasma waveguide, for the case $\omega_{pe} > \omega_{ce}$. Further investigation has required us to modify and elaborate on some of the statements made in the previous report.

We shall discuss the backward-wave interaction with the aid of numerical solutions to the dispersion equation. Collisions will be neglected in order to concentrate on the essential features. Under the assumption of quasi-static waves of the form $e^{j(\omega t-kz)}$, the dispersion equation reads[1]

$$(\omega-kv_o)^2\left[k^2\left(1-\frac{\omega_{pe}^2}{\omega^2}\right)+p^2\left(1-\frac{\omega_{pe}^2}{\omega^2-\omega_{ce}^2}\right)\right]=k^2\omega_b^2, \tag{1}$$

where k, p are the axial and transverse wave numbers in the waveguide, and ω_b is a reduced plasma frequency for the beam.[2]

In the following numerical examples, frequencies are expressed in units of ω_{pe} and wave numbers in units of (ω_{pe}/v_o). The value of (pv_o/ω_{pe}) will be fixed at 0.1 and $(\omega_{ce}/\omega_{pe})$ will be fixed at 0.5. The parameter (ω_b/ω_{pe}) will be varied, however, and we shall demonstrate how the nature of the instability changes as the beam density is increased.

Consider first a relatively weak beam, $(\omega_b/\omega_{pe}) = 0.01$. Figure XII-12a shows the locus of the complex roots of the dispersion equation in the ω-plane for positive real k (the roots lying on the real ω-axis have been omitted). This figure shows that instabilities are possible over essentially all frequencies near and below ω_{pe}. Figures XII-13a and XII-14a are similar plots, but for stronger beams, $(\omega_b/\omega_{pe}) = 0.03$ and 0.06, respectively. Except for differences in magnitudes of Im (ω/ω_{pe}), the three plots look quite similar, and all indicate possible instabilities in roughly the same range of frequencies. We wish to concentrate on the beam interaction with the backward plasma wave, which occurs near ω_{pe}.

Using the Bers-Briggs stability criteria,[3] we found the instabilities for the backward-wave interaction to be different for each of the three values of (ω_b/ω_{pe}) cited above. Figure XII-12b illustrates the application of the stability criteria to the case $(\omega_b/\omega_{pe}) = 0.01$. The following features may be noted in the complex k-plane: (i) for ω just below ω_{pe}, the slow space-charge wave is amplifying and the plasma waves are strongly evanescent; (ii) as ω passes through ω_{pe}, the two plasma roots switch from $k \approx \pm j\infty$ to $k \approx \pm\infty$, exhibiting the usual plasma resonance; (iii) at some frequency slightly above

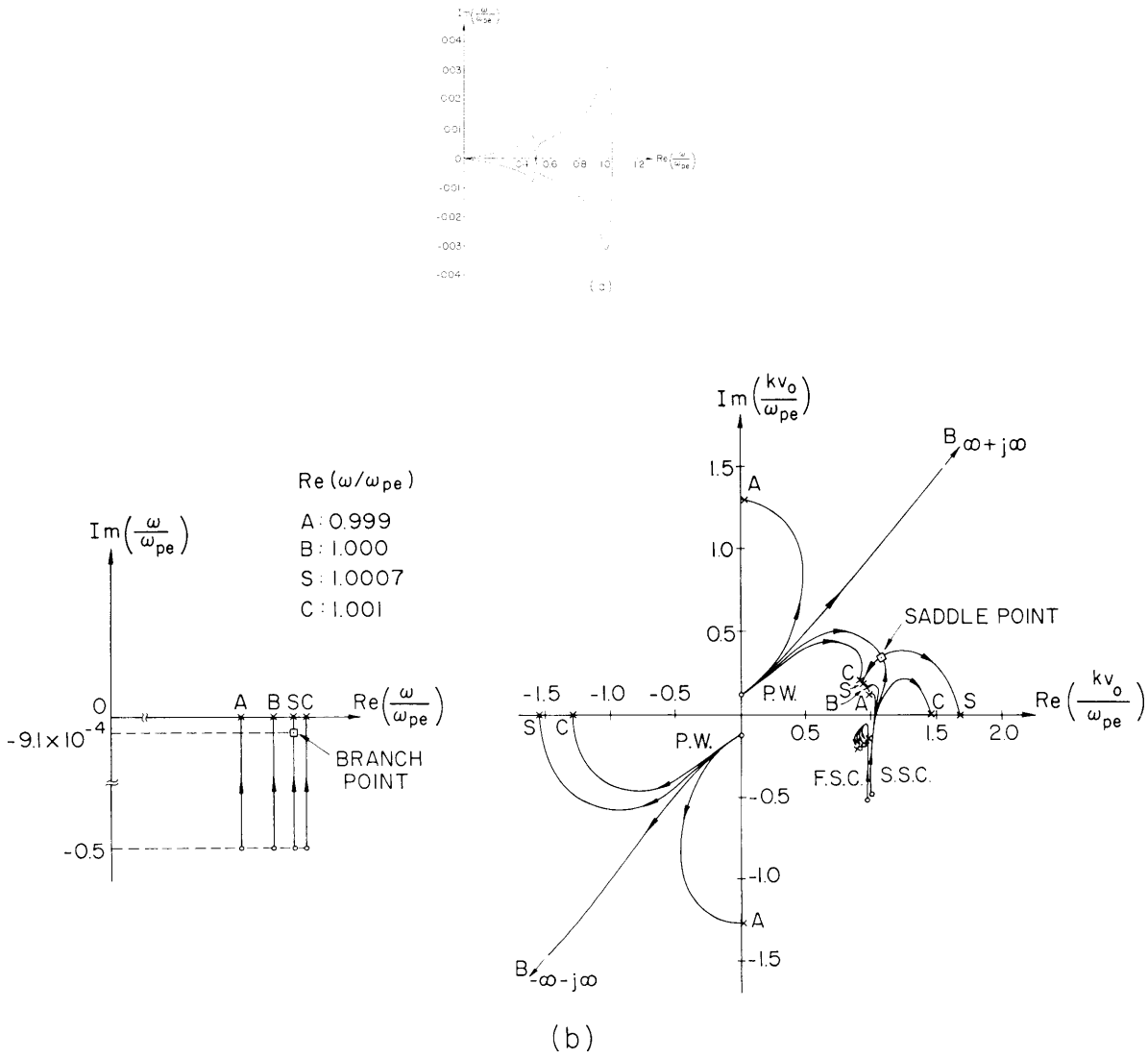

Fig. XII-12. (a) Locus of roots of the dispersion equation in the complex ω-plane for positive real k. Roots on the real ω axis have been omitted. Parameters: $pv_o/\omega_{pe} = 0.1$; $\omega_{ce}/\omega_{pe} = 0.5$; $\omega_b/\omega_{pe} = 0.01$.

(b) Application of stability criteria for the region near ω_{pe}, showing the locus of the roots of the dispersion equation in the complex k-plane as Im (ω) is varied as shown on the left. Waves are identified in the k-plane at large negative imaginary ω: P.W. = plasma wave; F.S.C. = fast beam space-charge wave; S.S.C. = slow beam space-charge wave. Parameters are the same as in (a).

Fig. XII-13. (a) Same as Fig. XII-12a, except that $\omega_b/\omega_{pe} = 0.03$.
(b) Same as Fig. XII-12b, except that $\omega_b/\omega_{pe} = 0.03$.

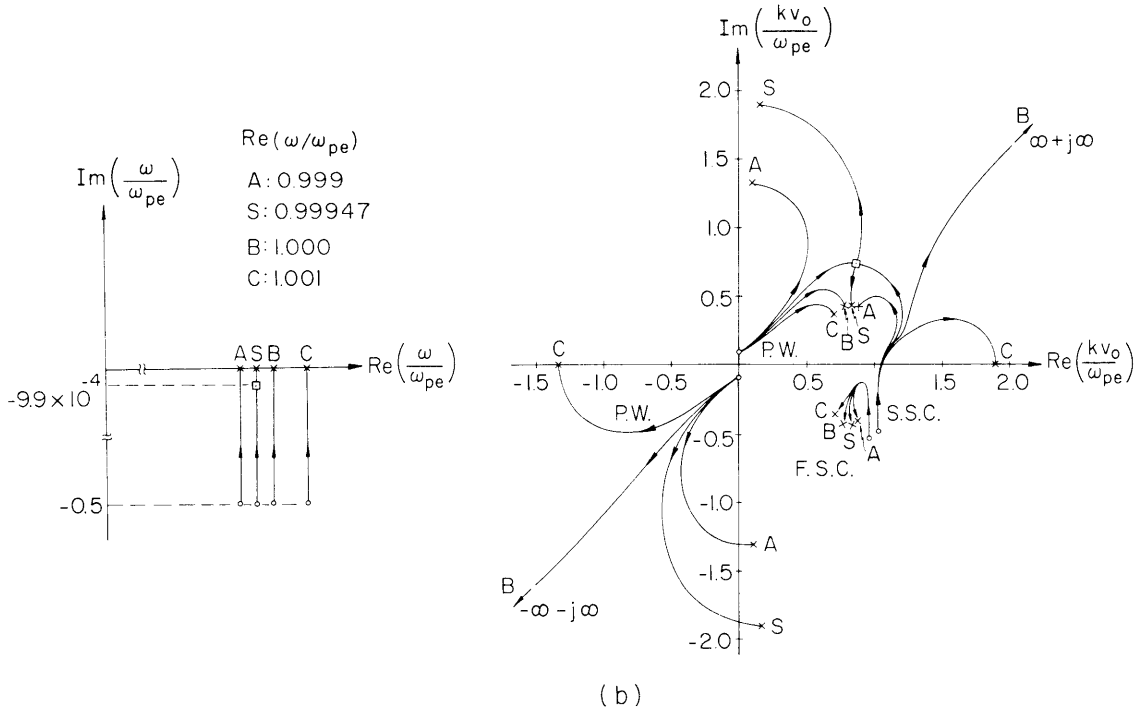

(b)

ω_{pe}, a saddle point, k_s, is formed by the merging of the plasma root from above and the slow beam-space-charge root from below. This indicates an absolute instability, and the corresponding branch point location, ω_s, is shown in the ω plane; (iv) at still higher frequencies, all waves are stable. The formation of the absolute instability for this weak-beam situation is just what one would expect from mode-coupling theory, by analogy with the backward-wave oscillator.

Consider next the case $(\omega_b/\omega_{pe}) = 0.03$, as illustrated in Fig. XII-13b. The branch point location for the absolute instability has shifted so that Re $(\omega_s) < \omega_{pe}$. For frequencies in the range Re $(\omega_s) < \omega < \omega_{pe}$, the slow space-charge wave becomes very strongly amplifying, and at ω_{pe} the amplification rate is infinite. This "infinite amplification rate" is due to an essential singularity of $k(\omega)$ at $\omega = \omega_{pe}$. The essential singularity is present even in the previous situation ($(\omega_b/\omega_{pe}) = 0.01$, Fig. XII-12), but there it gave rise to the stable plasma resonance. In evaluating the time-asymptotic response it is

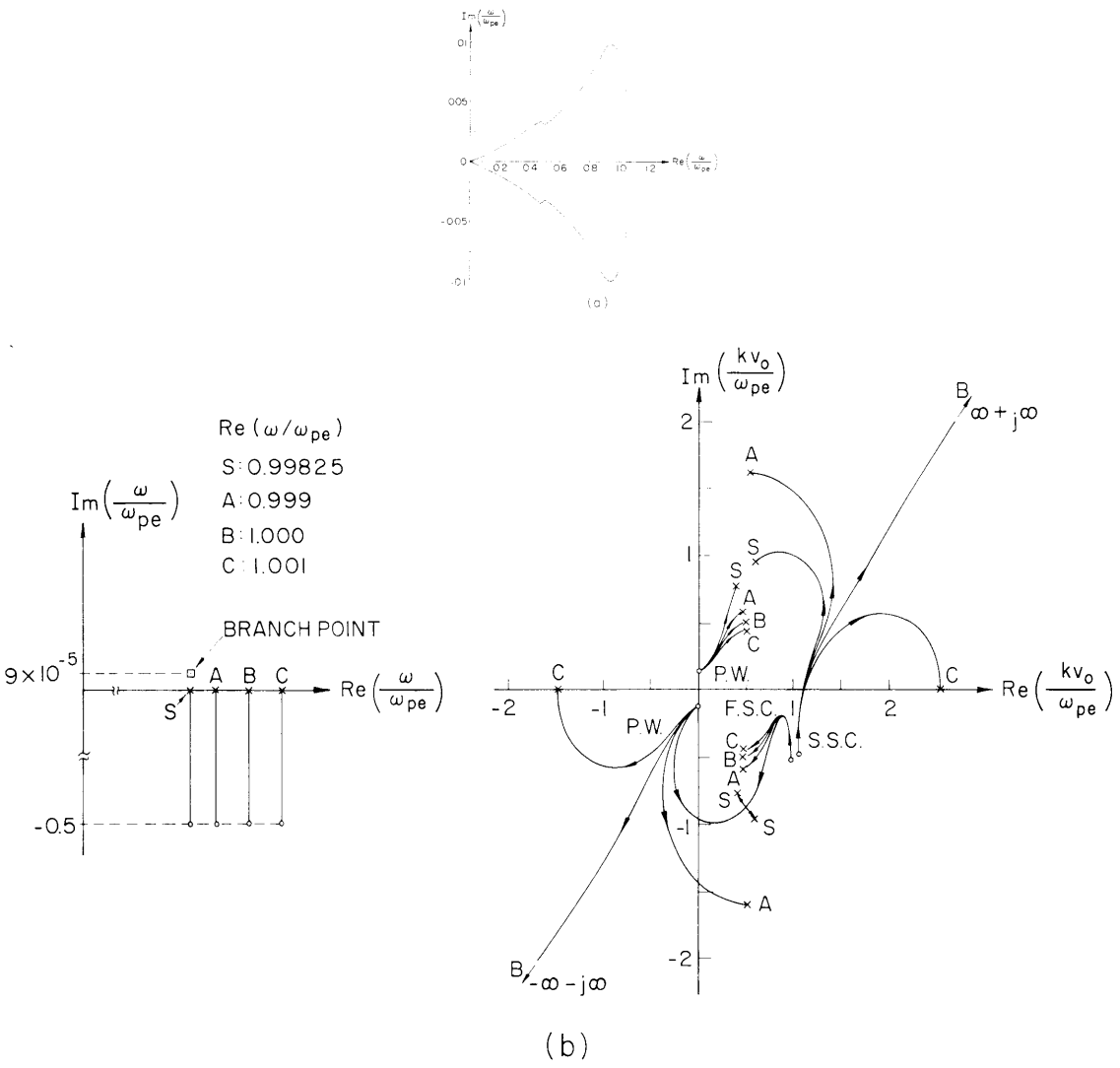

Fig. XII-14. (a) Same as Fig. XII-12a, except that $\omega_b/\omega_{pe} = 0.06$.
(b) Same as Fig. XII-12b, except that $\omega_b/\omega_{pe} = 0.06$.
The saddle formed in the lower half k-plane does not indicate an absolute instability.

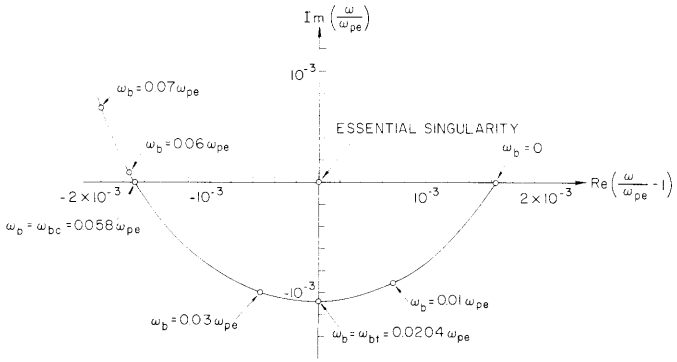

Fig. XII-15.

Locus of the relevant branch point in the complex ω-plane as ω_b is varied. When $\omega_b = \omega_{bt}$, the branch point lies directly below the essential singularity at ω_{pe}. Increasing ω_b further to ω_{bc} causes the branch point to cross into the upper half ω-plane.

necessary to consider this essential singularity, in addition to the branch pole at ω_s.

The case $(\omega_b/\omega_{pe}) = 0.06$ is shown in Fig. XII-14b. Here the absolute instability has disappeared. Investigation shows that the branch point ω_s has moved into the upper half ω-plane. Note that the essential singularity at $\omega = \omega_{pe}$ continues to give rise to an instability for the slow space-charge wave.

The way in which the instability changes with (ω_b/ω_{pe}) may be made clearer by plotting the locus of the branch point ω_s as a function of (ω_b/ω_{pe}) (see Fig. XII-14). Note that the branch point moves to the left as (ω_b/ω_{pe}) is increased. The branch point causes an "interchange" of k(Re(ω)) for those roots involved in the absolute instability. For $\omega_b < \omega_{bt}$ (Fig. XII-15) the interchange occurs for Re $(\omega) > \omega_{pe}$, and hence the plasma resonance is unaffected. When ω_b is increased beyond ω_{bt}, however, the interchange happens below ω_{pe} and in place of the plasma resonance there is now "infinite amplification" of the slow space-charge wave at ω_{pe}. As ω_b is increased even more, a critical value $\omega_b = \omega_{bc}$ is reached where the branch point crosses into the upper half ω-plane. The absolute instability then disappears. We have not found any further change in the nature of the instability for higher values of ω_b $(\omega_b < \omega_{pe})$.

Analysis of the dispersion equation shows that the branch point location ω_s satisfies the relation

$$\left(\frac{\omega_s}{\omega_{pe}}\right)^2 - 1 = -\left(\frac{pv_o}{\omega_{pe}}\right)^2 K_\perp(\omega_s)\left[1 + \left(\frac{\omega_b^2/\omega_{pe}^2}{-\left(\frac{pv_o}{\omega_{pe}}\right)^2 K_\perp(\omega_s)}\right)^{1/3}\right]^3, \tag{2}$$

where

$$K_\perp(\omega_s) = 1 - \frac{\omega_{pe}^2}{\omega_s^2 - \omega_{ce}^2}.$$

The right-hand side of Eq. 2 is usually small, so that an iterative procedure may be used to solve for ω_s (by setting $\omega_s = \omega_{pe}$ on the right-hand side as a first approximation). The equation yields several roots for (ω_s/ω_{pe}), but in the limit of very small (ω_b/ω_{pe}), only one of these roots has Re $(\omega_s) > \omega_{pe}$ and Im $(\omega_s) < 0$. The locus of this correct root can then be traced in the complex ω-plane as (ω_b/ω_{pe}) is increased.

In many cases of interest, the inequality

$$\left|\frac{\omega_s^2}{\omega_{pe}^2} - 1\right| \ll 1 - \frac{\omega_{ce}^2}{\omega_{pe}^2}$$

is satisfied, so that we may set $K_\perp(\omega_s) \approx K_\perp(\omega_{pe})$. The right-hand side of Eq. 2 may then be evaluated directly. With this approximation the expressions for ω_{bc} and ω_{bt} take the simple forms

$$\frac{\omega_{bc}}{\omega_{pe}} = \left(\frac{pv_o}{\omega_{pe}}\right)\sqrt{-K_\perp(\omega_{pe})} = \frac{\left(\frac{pv_o}{\omega_{pe}}\right)\left(\frac{\omega_{ce}}{\omega_{pe}}\right)}{\sqrt{1-\left(\frac{\omega_{ce}}{\omega_{pe}}\right)^2}} \tag{3}$$

$$\omega_{bt} = \frac{1}{\sqrt{8}}\,\omega_{bc} = 0.354\,\omega_{bc}. \tag{4}$$

Equation 3 was given in our last report. These expressions hold with good accuracy for the numerical example presented above. A more general analysis for nonzero (pv_o/ω_{pe}) and $0 < (\omega_{ce}/\omega_{pe}) < 1$ shows that ω_{bt} is always less than ω_{bc}.

From the foregoing discussion it is evident that the backward-wave beam-plasma interaction is much more complicated than one would expect by analogy with the backward-wave oscillator. In particular, the important role of the essential singularity appears to have been neglected hitherto, and its physical significance (when collisions and temperature effects are taken into account) still remains to be found. The growth in space and time of instabilities characterized by adjacent branch point and essential singularities in the complex-ω plane also needs to be studied.

S. L. Chou, A. Bers

References

1. S. Chou and A. Bers, "Beam Space-Charge-Wave Interaction with the Backward Wave in a Cold-Plasma Waveguide," Quarterly Progress Report No. 88, Research Laboratory of Electronics, M.I.T., January 15, 1968, pp. 183-185.
2. S. Chou and A. Bers, "Thin Electron-Beam Interactions with Ions in a Plasma-Filled Waveguide," Quarterly Progress Report No. 87, Research Laboratory of Electronics, M.I.T., October 15, 1967, pp. 89-99.
3. R. J. Briggs, Electron-Stream Interaction with Plasmas (The M.I.T. Press, Cambridge, Mass., 1964).

7. GROWTH OF THE LOSSLESS, ONE-DIMENSIONAL BEAM-PLASMA INTERACTION IN SPACE AND TIME

We find the growth in space and time of v_b, the first-order beam velocity, in a system described by the dispersion relations

$$1 - \frac{\omega_p^2}{\omega^2} - \frac{\omega_{pb}^2}{(\omega - kv_o)^2} = 0. \tag{1}$$

Briggs[1] has obtained an asymptotic solution to the transient response of a system described by Eq. 1 by the saddle-point method. He left out some multiplicative and phase factors, however, which we need for a quantitative comparison with our computer experiments.[2]

At $z = 0$ we impose a velocity modulation on the beam at ω_p, but no beam density modulation, starting at $t = 0$. That is,

$$v_b(z=0) = v_{bac} \sin \omega_p t u_{-1}(t), \tag{2}$$

where v_{bac} is the magnitude of the modulation, and u_{-1} is the unit step function. We choose $v_{bac} = -10^{-4} v_o$, a value small enough to allow v_b to become large relative to the modulation, so the asymptotic theory can be valid, but still to be linear. We shall show that a source electric field of the form

$$E_s(t, z) = E_o \delta(z)\, tu_{-1}(t) \tag{3}$$

will produce the required beam modulation, where E_o is in units of electric field times velocity. The transform of E_s is given by

$$E_s(\omega, k) = \int_0^\infty dt \int_{-\infty}^\infty dz\, e^{-j(\omega t - kz)}\, E_s(t, z),$$

or

$$E_s(\omega, k) = -E_o/\omega^2. \tag{4}$$

The total electric field generated by E_s in the beam-plasma system is given by

$$E(\omega, k) = \frac{\rho_b + \rho_p}{-jk\epsilon_o} + E_s, \tag{5}$$

in which we have used the transform of Gauss' law, and have assumed that ρ_b and ρ_p, the first-order beam and plasma charge densities, respectively, are generated by the total electric field, but that E_s is generated by an external source.

The total electric field is

$$E(\omega, k) = \frac{E_s(\omega, k)}{1 - \frac{\omega_p^2}{\omega^2} - \frac{\omega_{pb}^2}{(\omega - kv_o)^2}}, \tag{6}$$

and the first-order beam velocity is given by

$$v_b(t, z) = -\frac{1}{(2\pi)^2} \int_{-\infty - j\sigma}^{\infty - j\sigma} d\omega \int_{-\infty}^{\infty} dk\, e^{j(\omega t - kz)} \frac{(q/m)E_o}{j\omega^2(\omega - kv_o)\left[1 - \frac{\omega_p^2}{\omega^2} - \frac{\omega_{pb}^2}{(\omega - kv_o)^2}\right]}. \tag{7}$$

We perform the integration in the k-plane first. If Im $\omega \to \infty$, all poles in the k-plane lie below the real k axis. Hence, by the Bers-Briggs criterion,[3] the contour of integration in the k-plane is above these poles. For $z > 0$ we close the contour below the real k axis. Some of the terms in Eq. 7 can be integrated in the ω-plane. By causality, all poles in the ω-plane lie above the ω contour. After canceling terms, the result is

$$v_b(t, z) = -\frac{qE_o}{mv_o 2\pi} \int_{-\infty - j\sigma}^{\infty - j\sigma} d\omega\, e^{j\omega(t - z/v_o)} \frac{\cos K(\omega)\, z}{\left(\omega^2 - \omega_p^2\right)}, \tag{8}$$

where $K(\omega) \equiv k_b\left(1 - \omega_p^2/\omega^2\right)^{-1/2}$, and $k_b \equiv \omega_{pb}/v_o$. At $z = 0$ the integral can be performed by contour integration. The result is

$$v_b(t, z=0) = \frac{qE_o}{mv_o\omega_p} \sin \omega_p(t)\, u_{-1}(t), \tag{9}$$

which agrees with Eq. 2, with $v_{bac} = -qE_o/mv_o\omega_p$.

For $z > 0$ the essential singularity at $\omega = \omega_p$ prevents integration of Eq. 8 by Cauchy's theorem. The saddle-point method[4] can be used, however. For an integral of the form $\int_c e^{f(t)}\, dt$ we have

$$\int_c e^{f(t)}\, dt \approx e^{f(t_o)} \sqrt{2\pi / e^{i\pi} f''(t_o)}. \tag{10}$$

The function $\phi(\omega) = \omega\tau - K(\omega)\, z$, where $\tau \equiv t - z/v_o$, has saddle points[1] at

$$\omega_s = \pm\omega_p \left\{1 + (k_b z/\omega_p \tau)^{2/3}\, e^{-j2\pi/3}\right\}^{1/2}. \tag{11}$$

We need

$$K(\omega_s) = k_b\left(1-\omega_p^2/\omega_s^2\right)^{-1/2} = k_b \frac{\omega_s}{\omega_p} e^{+j\pi/3}\left[\frac{k_b z}{\omega_p \tau}\right]^{1/3}, \tag{12}$$

and

$$K''(\omega_s) = \frac{3k_b\omega_s^3}{\left(\omega_s^2-\omega_p^2\right)^{5/2}} = \frac{3k_b\omega_s^3}{\omega_p^5\left[\frac{k_b z}{\omega_p \tau}\right]^{5/3} e^{-j5\pi/3}}. \tag{13}$$

Hence Eq. 8, after adding the contributions at both saddle points, is approximately

$$v_b(t, z) \approx -\frac{qE_o}{mv_o\sqrt{6\pi k_b z}} \frac{F^{1/6}\, e^{\mathrm{Re}\,(j\omega_s - jK(\omega_s)z)} \cos(\theta)\, u_{-1}(\tau)}{(1-F^{2/3}+F^{4/3})^{3/8}}, \tag{14}$$

where $F = (k_b z/\omega_p \tau)$, and

$$\theta = \mathrm{Re}\left\{\omega_s\tau - K(\omega_s)z\right\} - 17\pi/12 + \frac{3}{4}\tan^{-1}\left\{\frac{\frac{3^{1/2}}{2}F^{2/3}}{\left(1-\frac{1}{2}F^{2/3}\right)}\right\}. \tag{15}$$

For $F = k_b z/\omega_p \tau \ll 1$, Eq. 14 reduces to

$$v_b(t, z) \approx -\frac{qE_o}{mv_o} \frac{e^{\left\{(3\sqrt{3}/4)(k_b z)^{2/3}(\omega_p\tau)^{1/3}\right\}}}{\sqrt{6\pi k_b z}} (k_b z/\omega_p\tau)^{1/6}$$

$$\times \cos\left\{\omega_p\tau - \frac{3}{4}(k_b z)^{2/3}(\omega_p\tau)^{1/3} - 17\pi/12\right\} u_{-1}(\tau). \tag{16}$$

In Fig. XII-16, Eq. 14 is compared with the snapshot of the beam velocity of the computer experiment[2] at $t = 150/\omega_p$. The beam is modulated at $z = 0$ so that

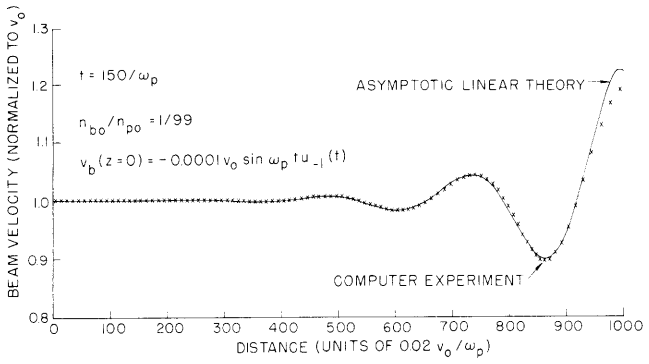

Fig. XII-16.

Snapshot comparing the beam sheet velocity of the computer experiment with that of the asymptotic linear theory.

$v_b(z=0) = -10^{-4}\ v_o \sin(\omega_p t)\ u_{-1}(t)$. For small values of v_b/v_o, the asymptotic theory is invalid. For v_b/v_o too large, the linear assumptions are invalid. There is a region in Fig. XII-16 in which $0.005 < |v_b/v_o| < 0.05$ where the asymptotic theory and the computer experiment agree quite well, except for a phase shift of order $\pi/30$.

J. A. Davis

References

1. R. J. Briggs, "The Effect of Essential Singularities on Stability Criteria," Quarterly Progress Report No. 85, Research Laboratory of Electronics, M.I.T., April 15, 1967, p. 183.

2. J. A. Davis, "Computer Models of the Beam-Plasma Interaction," Quarterly Progress Report No. 87, Research Laboratory of Electronics, M.I.T., October 15, 1967, p. 81.

3. R. J. Briggs, Electron-Stream Interactions with Plasma (The M.I.T. Press, Cambridge, Mass., 1964), p. 32.

4. P. M. Morse and H. Feshbach, Methods of Theoretical Physics, Vol. 1 (McGraw-Hill Book Company, New York, 1953), p. 437.

XII. PLASMAS AND CONTROLLED NUCLEAR FUSION*

B. Applied Plasma Physics Related to Controlled Nuclear Fusion

Academic and Research Staff

Prof. T. H. Dupree
Prof. E. P. Gyftopoulos
Prof. L. M. Lidsky
Prof. N. L. Oleson
Prof. S. Yip
Prof. T. O. Ziebold
Dr. R. A. Blanken

Graduate Students

J. D. Callen
D. G. Columbant
C. T. Dum
R. E. Fancher
R. W. Flynn
M. Hudis
M. A. Le Comte
G. R. Odette
D. H. Ross
A. Sugawara
C. E. Wagner

1. RADIATION DAMAGE IN THERMONUCLEAR REACTORS

It has been pointed out that radiation damage to the components of proposed thermonuclear reactors might present very serious engineering problems.[1] There is no sufficiently strong source of 14-MeV neutrons (which are produced in the D(T,n)α reaction) to make practical realistic engineering tests. Therefore a study has been undertaken to modify basic damage theory and to extend it to this energy range. Furthermore, an experimental technique has been developed to directly compare the relative effects on the anelastic properties of copper single crystals of reactor irradiations in the Massachusetts Institute of Technology Reactor (MITR) and in 14-MeV neutron bombardment from a Cockroft-Walton neutron generator. Anelastic properties such as internal friction are of the order of 10^5 times more sensitive to defect concentration than are other mechanical or physical properties, such as macroscopic yield strength or electrical resistance. It was the general aim of this work, by using both experimental and theoretical analysis, to develop more accurate models of the energy dependence of neutron radiation damage and to use these results for extrapolation of the relatively abundant reactor data to 14 MeV.

Theory and Analysis

The major mechanical property effect of neutron irradiation on metals is to strengthen and embrittle them. At low temperatures the major contribution to this is due to displacement damage resulting from fast neutron scattering events.

The assumption that is usually made is to consider all of the scattering isotropic and elastic in nature. This can lead to very serious errors in the calculation of the primary knockon atom spectra, K(T), especially at high neutron energies. Therefore, in

*This work was supported principally by the National Science Foundation (Grant GK-2581).

this work, K(T) was calculated by using experimentally measured differential scattering cross sections. The nonelastic scattering was accounted for by making the approximation that its behavior is elastic and isotropic in nature. These calculations were carried out for Cu and Mo at several neutron energies. Also, K(T) for representative reactor irradiations was approximated by breaking the neutron spectrum into several energy groups, determining $K_i(T)$ for average energies in these groups, and summing after proper flux weighting.

One measure of the amount of radiation damage is the total number of displaced atoms. An energetic primary knockon atom (PKA), before it comes to rest, produces many generations of displaced atoms over a region of the lattice known as a displacement cascade. This region has a lateral dimension of the order of 100 Å. The total displacement cross section, σ_d, can be calculated from

$$\sigma_d = \int_0^{T_m} \nu(T)\, K(T)\, dT, \tag{1}$$

where T_m is the maximum PKA energy, and $\nu(T)$ is the total number of displacements resulting from a PKA of energy T.

It is evident that the distribution, as well as the total number of defects, will influence the nature of radiation damage. The most widely accepted explanation of radiation hardening in metals was developed by Seeger[2] at Stuttgart, and later modified and extended by other workers. He postulated the hardening defect to be a small region, approximately 10 Å in diameter, containing a large excess of vacancies. From simple dislocation theory the yield stress would be expected to increase as the square root of the total number of such zones. Computer simulations of the cascade also predict the presence of large vacancy clusters dispersed in the cascade. The estimate of the minimum number of vacancies in a cluster needed to effectively inhibit the motion of dislocations is 10. Based on the results of Beeler's[3] calculations, a zone cross section, σ_z, was defined from

$$\sigma_z = \int_{E_t}^{T_m} f(T)\, \nu(T)\, K(T). \tag{2}$$

The zone is assumed to be a cluster of 10 or more vacancies, and E_t, the threshold energy needed to form a zone, was taken to be 2.5 keV. Above this threshold energy, f(T) is approximately a constant factor.

In this model a random distribution of hardening obstacles is assumed. Although the cascades are randomly spaced, the zones themselves will be clustered if the cascades contain more than one zone. Our calculations, based on simple models, indicated that multiple zone cascades would occur at sufficiently high PKA energies and,

furthermore, that the effective strain volumes of these spikes would overlap in some instances. For a third model we postulated that the cascade as a whole could serve as a dislocation barrier. Approximate calculations based on cascade

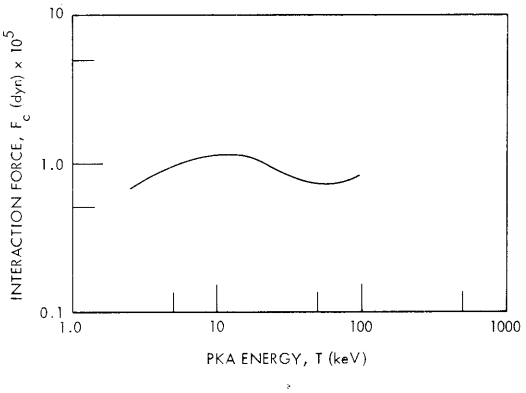

Fig. XII-17. Characteristic cascade-dislocation interaction force in Mo.

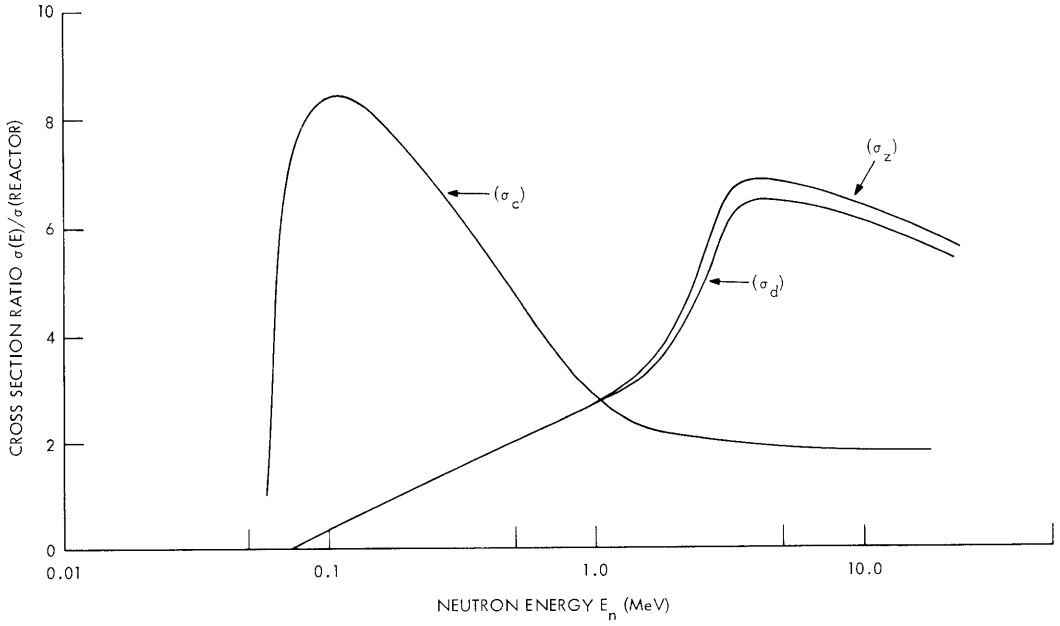

Fig. XII-18. Damage cross-section ratios.

strain energy and dimensions demonstrated a relative intensity of the cascade's ability to hinder dislocation motion to the PKA energy, as shown in Fig. XII-17. Thus, a third cross section based on the formation of effective cascades, σ_c, was defined as

Table XII-1. Summary of damage parameters.

Material	Neutron Energy (MeV)	σ_s (barns)	T_{max} (keV)	$\overline{T}$ (keV)	σ_d (barns)	$\frac{\sigma_d(E)}{\sigma_d(E_r)}$	σ_z (barns)	$\frac{\sigma_z(E)}{\sigma_z(E_r)}$	σ_c (barns)	$\frac{\sigma_c(E)}{\sigma_c(E_r)}$
Cu	Reactor Spectrum	4.6	–	5.0	455	1.00	1.54	1.00	1.6	1.00
Cu	0.1	8.0	6.25	3.1	520	1.14	1.74	1.13	3.25	2.03
Cu	0.5	4.5	31.3	14.0	1270	2.81	4.8	3.12	4.5	2.81
Cu	1.5	3.3	93.8	38.4	2190	4.80	8.65	5.62	6.0	3.75
Cu	3.7	3.3	231.3	87.0	2720	5.97	10.8	7.01	1.6	1.0
Cu	14.	3.2	875.	238.0	2445	5.37	9.8	6.36	1.7	1.06
Mo	Reactor Spectrum	8.4	–	3.9	439	1.00	1.64	1.00	0.7	1.0
Mo	0.1	8.6	4.16	2.0	230	0.52	0.59	0.36	6.0	8.57
Mo	0.5	8.1	20.8	7.2	841	1.92	3.34	2.04	4.0	5.71
Mo	1.5	7.0	41.7	13.7	1290	2.94	5.17	3.15	3.2	4.57
Mo	3.7	4.0	184.2	60.0	2841	6.47	11.4	6.95	1.6	2.29
Mo	14.	3.8	583.3	165.0	2520	5.76	10.1	6.16	1.3	1.86

$$\sigma_c = \int_{E_t}^{T_m} K(T)\, dT, \tag{3}$$

with E_t again taken as 2.5 keV.

The displacement, zone and cascade cross sections were calculated by graphical integration, with the Kinchen and Pease[4] model for $\nu(T)$ used. The results are summarized in Table XII-1. The ratios of the cross sections are more significant than the cross sections themselves, since many of the assumed constants and approximations are canceled out in this process. A plot of these ratios for monoenergetic to reactor spectrum irradiations is shown in Fig. XII-18. If the effect of saturation at high doses is neglected, the ratio of damage rates simply reduces to $\sqrt{\sigma(E)/\sigma(\text{reactor})}$. The cascade cross section is recommended for extrapolation over large energy ranges; on this basis, damage for 14-MeV irradiation would be expected to be approximately 1.5 times that for equivalent irradiation in a well-moderated reactor spectrum. Future work includes refinement of the models and development of computer codes for numerical calculations.

Experimental Work

Apparatus was built to measure changes in the anelastic properties of Cu single crystals as a function of fast neutron exposure at room temperature. Bombardments were made in both 14-MeV and reactor spectrum fluxes to determine their relative effectiveness in producing dislocation pinning points. The stress-induced motion of free dislocation lengths ($\underline{\ell}$) between pinning points has two major consequences, owing to in- and out-of-phase components. The former leads to a difference between the measured and purely elastic modulus ($\Delta G/G$), which is known as the modulus defect, while the latter leads to damping or internal friction. The behavior of these parameters causes a division into two regions – strain-independent and strain-dependent. The strain-dependent region is thought to be due to progressive dislocation breakaway from pinning points. The usual parameter for representing internal friction is the logarithmic decrement (δ), which for a driven system is defined as half the ratio of irreversible energy loss to the total oscillator energy per cycle.

Formal internal friction theory predicts a fourth-power dependence of δ on $\underline{\ell}$, with $\Delta G/G$ being proportional to the square of this length. The effect of irradiation is to add pinning points (n_r) that shorten the average length as $\underline{\ell} = 1/(n_r+n_o)$, where n_o is the pre-irradiation number of pinning points. Thus two experimental parameters can be defined to measure the ratio of n_r/n_o as

$$n_r/n_o = (Y^{-1/2}-1) = (Z^{-1/4}-1), \tag{4}$$

where

$$Y = \left(\frac{\Delta G}{G}\right) \Big/ \left(\frac{\Delta G}{G}\right)_o = (\underline{\ell}/\underline{\ell}_o)^2 = (1+n_r/n_o)^{-2} \tag{5}$$

and

$$Z = \delta/\delta_o = (\underline{\ell}/\underline{\ell}_o)^4 = (1+n_r/n_o)^{-4}. \tag{6}$$

Here, n_r is a function of neutron exposure:

$$n_r = \text{const} \times f(\phi t \sigma). \tag{7}$$

To a first-order approximation the number of pinning points was taken to be directly proportional to the number of defects induced throughout the lattice. Thus

$$n_r = \text{const} \times (\phi t \sigma_d). \tag{8}$$

The constant in Eq. 8 is a function of time, temperature, and defect mobilities. A measure of the defect production cross section is found from

$$\frac{dn_r}{d(\phi t)} = \text{const} \times \sigma_d. \tag{9}$$

If the experimental conditions are kept constant, the relative damage effectiveness of 14 MeV to reactor irradiations is simply a ratio of the slopes found from Eq. 9.

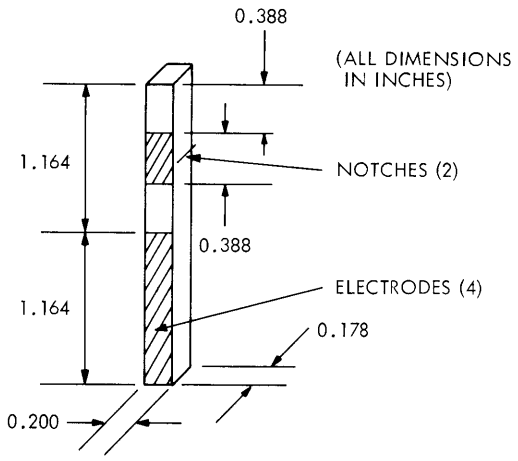

Fig. XII-19. Quartz resonator.

The design of the internal friction spectrometer was based on the concept of a composite resonator. It is composed of a frequency-matched driver, gauge, and specimen crystals. The modulus was determined from the resonant frequency of the system, and the strain amplitude and decrement from the driver and gauge voltages. The driver and gauge are composed of a single -18.5 X-cut alpha quartz crystal with a resonant frequency of 85,125 Hz and adherent Cu electrodes. The physical configuration of the resonator is shown in Fig. XII-19 and its support and housing in Fig. XII-20. Original calibration for the system was made using a radio frequency bridge. A block diagram of the electronic system is shown in Fig. XII-21. The Cu crystals were grown in graphite molds from high purity Cu rod, with the use of the

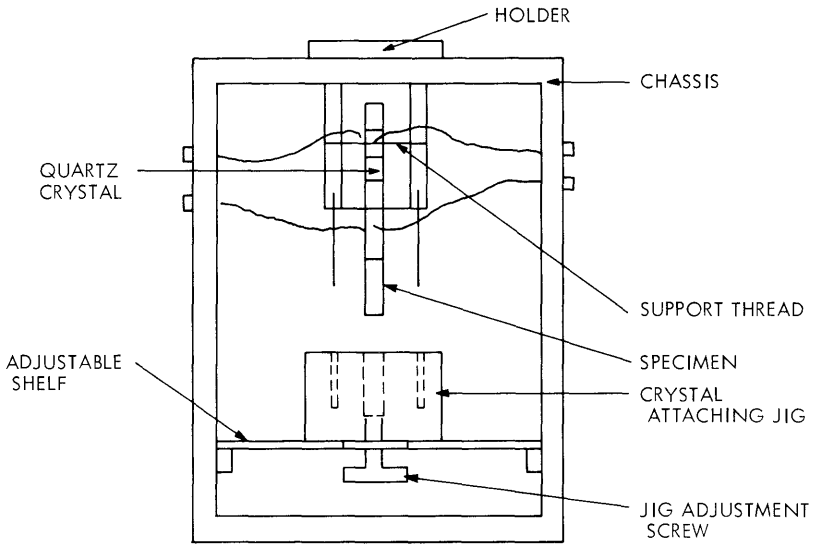

Fig. XII-20. Resonator support and housing.

Bridgeman method, and were reduced to the proper length after their crystallographic orientation had been determined in a series of operations involving cutting with a jewelers saw, carefully polishing the ends, and lightly etching. They were then vacuum-annealed at 800°C for 24 hours and allowed to furnace cool. The sample was attached to the quartz resonator with glue of low melting point, and care was taken to keep the

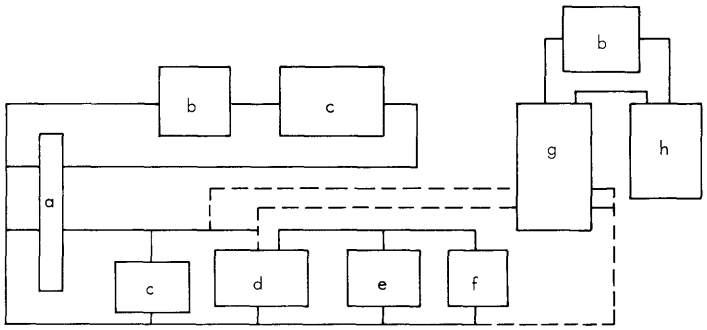

Fig. XII-21. Experimental system (dotted lines for calibration).

strain level as low as possible. All measurements were made at a strain of 5×10^{-8}, which was found to be in the strain-independent region.

Reactor irradiations were carried out in position 13 of the MITR for very short times while it operated at low power. The flux was monitored with nickel threshold detectors. The 14-MeV irradiations were made with a Texas Nuclear Cockcroft-Walton neutron generator using the D-T reaction, and the high-energy flux was monitored with a plastic scintillation detector. The reactor irradiations were made only on the Cu sample, while the 14-MeV irradiations were made with the whole system in place because it was found that repeated handling of the samples caused more error than that resulting from irradiation of the quartz. After all irradiations at least 24 hours was allowed for property changes to approach equilibrium before the measurements were made.

A summary of the initial experimental results is given in Table XII-2, and plots of δ and G as a function of neutron dose are given in Fig. XII-22. The ratio n_r/n_o is plotted

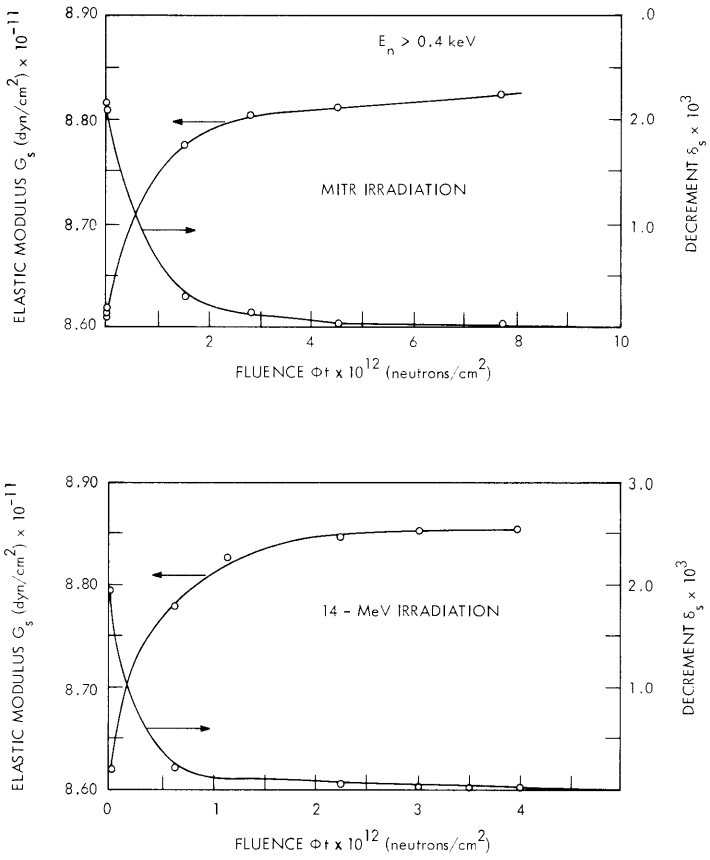

Fig. XII-22. Effect on anelastic properties of fast neutron irradiations.

in Fig. XII-23. From Eqs. 4, 5, 6 and the experimental data, $dn_r/d(\phi t)$ was found to be 0.145 for 14-MeV irradiation and 0.04 for the reactor irradiation. With the use of Eq. 9, this gives a ratio of 3.6 for the 14 MeV-to-reactor displacement cross sections. This can

Table XII-2. Summary of experimental results.

A. For reactor irradiations.*

ϕt†	$\delta \times 10^2$	$G \times 10^{-11}$	$Z^{-1/4} - 1$	$Y^{-1/2} - 1$
Annealed	2.14	8.614		
Annealed	2.02	8.617	0	0
Annealed	2.09	8.609		
1.46×10^{12}	3.27×10^{-1}	8.758	0.59	0.58
2.73×10^{12}	8.32×10^{-2}	8.805	1.24	1.23
4.48×10^{12}	3.37×10^{-2}	8.825	1.82	1.80
7.60×10^{12}	8.05×10^{-3}	8.843	3.00	3.10

B. For 14-MeV irradiations.**

ϕt	$\delta \times 10^2$	$G \times 10^{-11}$	$Z^{-1/4} - 1$	$Y^{-1/2} - 1$
Annealed	2.16	8.621	0	0
0.6×10^{12}	1.84×10^{-1}	8.781	0.85	0.85
1.12×10^{12}	4.30×10^{-2}	8.826	1.65	1.64
2.24×10^{12}	6.11×10^{-3}	8.847	3.30	3.28
2.80×10^{12}	3.70×10^{-3}	8.850	4.00	3.90
3.28×10^{12}	2.38×10^{-3}	8.852	4.65	4.50

*Crystal 1A – m_s = 2.251 g; l_s = 0.7251"; d_s = 0.164"; $F(\alpha)$ = 0.118.

**Crystal 1B – m_s = 2.259 g; l_s = 0.7256"; d_s = 0.164"; $F(\alpha)$ = 0.118.

†All integrated fluxes above energy of 400 eV.

be compared with an analytical calculation by using the techniques described in the previous section of 4.3. These results are in surprisingly good agreement,

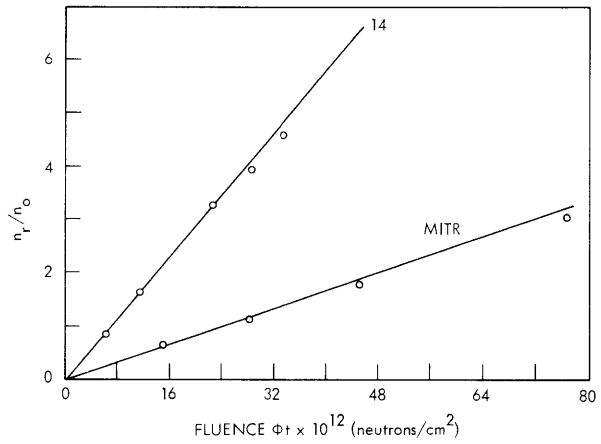

Fig. XII-23.
Radiation-induced pinning points.

in view of the rather large experimental and theoretical uncertainties involved.

Future experimental work will involve improvement of the apparatus in terms of sensitivity and accuracy. Additional experiments under similar conditions will help to demonstrate the reproducibility of the results. We also plan to make measurements for both amplitude-dependent and amplitude-independent strains at different temperatures, since these should prove valuable in studying the nature of both the radiation-induced and pinning defects.

G. R. Odette, T. O. Ziebold

References

1. G. R. Odette, "Development of Radiation Damage Models for High Energy (14 MeV) Neutrons," S.M. Thesis, M.I.T., January 1968.
2. A. Seeger, P/2385, Proc. Second International Conference on the Peaceful Uses of Atomic Energy, Vol. 6 (United Nations, 1958), 274.
3. J. Beeler, "Absolute Number of Defect Clusters Produced on Neutron Irradiated α-Iron per Unit Exposure," GE-TM 65-12-14, 1965.
4. G. Kinchen and R. Pease, Rept. Progr. Phys. 18, 1 (1955).

XII. PLASMAS AND CONTROLLED NUCLEAR FUSION

C. Active Plasma Effects in Solids*

Academic and Research Staff

Prof. A. Bers
Prof. G. Bekefi
Prof. S. K. Sharma
Dr. W. M. Manheimer

Graduate Students

S. R. J. Brueck
E. V. George
C. W. Hartman
D. A. Platts
J. H. Spencer
R. N. Wallace

1. EFFECTS OF CONTACTS ON LOW-FIELD MICROWAVE EMISSION FROM INDIUM ANTIMONIDE LOOPS WITH INDUCED ELECTRIC FIELDS

Introduction

This report describes further experimental observations of low-field microwave emission from loop-shaped samples of n-InSb. The basic experiment, which was described in a previous report,[1] differs from the experiments of other workers,[2-6] in that electric fields are induced in the sample by means of a time-variant magnetic field, rather than applied to the sample directly through ohmic contacts. The results of recent experiments modify to some extent the conclusions previously reported.[1]

System Modifications

A new waveguide structure and RF magnetic field coil were used for the experiments presented here; otherwise the apparatus is unchanged. Figure XII-24 shows a detailed

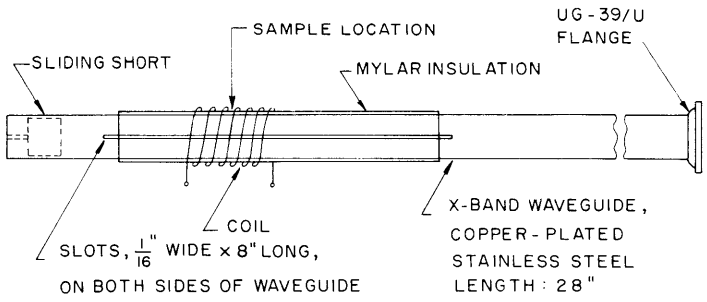

Fig. XII-24. Waveguide and RF magnetic field coil.

*This work was supported principally by the National Science Foundation (Grant GK-2581).

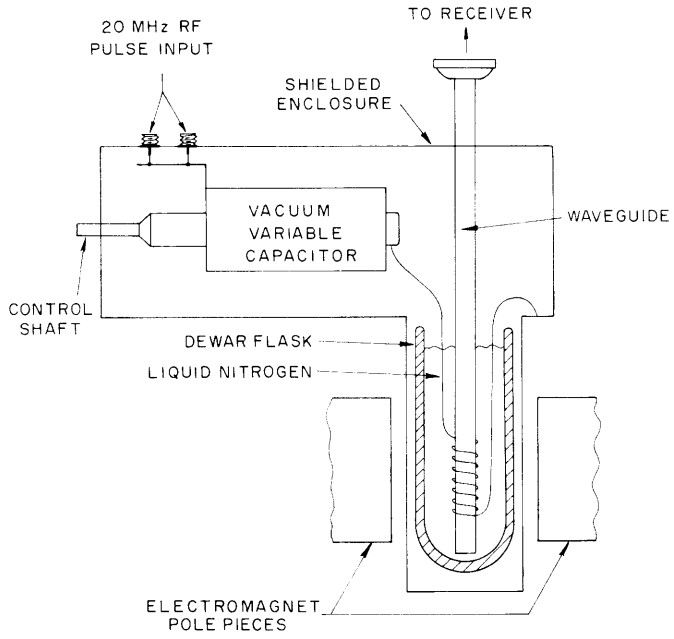

Fig. XII-25. Schematic representation of the complete waveguide and RF magnetic field system. This system replaces the one shown in Figs. IX-43 and IX-44 of the previous report.

view of the waveguide and coil, while Fig. XII-25 provides a schematic representation of the complete system. The coil, which has an inductance near 2 μH, consists of 13.5 turns of No. 16 formvar-insulated wire covered by No. 14 polyvinychloride tubing and No. 10 teflon tubing. It is further insulated from the waveguide by 11 layers of .005-inch mylar sheet. The X-band waveguide is made of copper-plated stainless steel.

The waveguide and coil are mounted in a shielded enclosure with the lower portion of the waveguide extending into a dewar flask that is filled with liquid nitrogen. The liquid nitrogen flows freely into the interior of the waveguide and comes into direct contact with the sample. The coil and InSb sample are thus maintained at 77°K during operation. The coil is adjusted for resonance at 20 MHz by means of a vacuum variable capacitor. Samples are supported in the waveguide by a system of mylar strips as shown in Fig. IX-42 of the previous report.[1]

This system offers a number of advantages over the earlier one. First, the dewar flask provides superior thermal isolation of the waveguide structure and sample so that less liquid nitrogen is consumed in operation. A sample temperature of 77°K may be assumed in this system with far more confidence. Second, the additional insulation provided by the liquid nitrogen surrounding the coil allows higher induced fields (~50 V/cm) to be achieved before breakdown of the coil structure occurs. Third, the absence of windows across the waveguide has made the sample more accessible, thereby speeding

sample-changing procedures. The microwave structure has fewer perturbations and offers the possibility of reduced reflections and reduced microwave losses. Finally, the rise time of the induced electric field has been reduced to approximately 3 μsec, and hence permits use of shorter RF pulses. This reduction in rise time occurred fortuitously as dielectric losses in the liquid nitrogen surrounding the coil reduced its Q below the level previously achieved. Somewhat higher RF power must be used to accommodate these additional losses.

Experimental Work

Square loops were cut from single crystals of n-InSb having an electron density of 10^{14} per cm^3 and a mobility of 6×10^5 cm^2/V-sec. The dimensions and crystallographic orientation of these samples are as shown in Fig. IX-40 of the previous report.[1] There were some minor differences in dimensions from sample to sample, because of the limited precision of the sample-cutting technique. The methods of sample fabrication and surface treatment were identical to those used previously.

The samples were mounted, as before, in the transverse plane of an X-band waveguide. The $[\bar{1}10]$ axis could be oriented either parallel to or perpendicular to the dominant mode electric field of the waveguide. A static magnetic field was applied in the

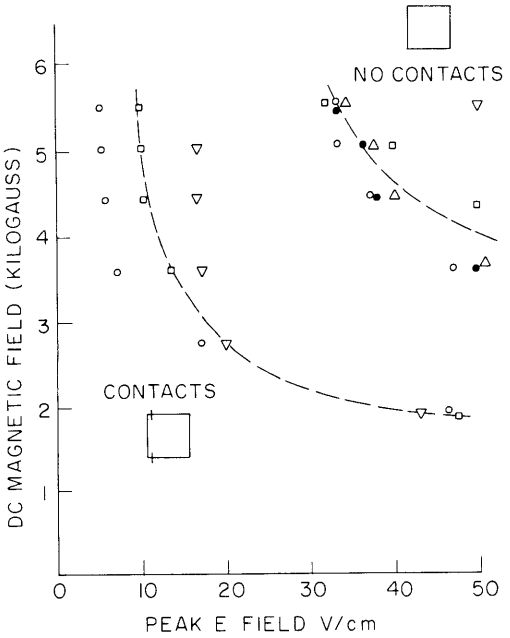

Fig. XII-26. Threshold electric and magnetic fields for microwave emission from loop samples with and without contacts. Samples tested: 3 with contacts, 5 without. Frequency of the observation: 9.5 GHz. 20-MHz RF pulse: 50 pps, 50-μsec duration. Emission threshold: ~200°K equivalent noise temperature.

plane of the sample along a diagonal of the square.

Several samples were tested to determine the values of electric and magnetic fields for which microwave emission could just be detected. The emission at this "threshold"

level corresponded to a noise temperature of roughly 200°K. Composite data for 5 different samples are shown in Fig. XII-26. Data are shown for a receiver frequency of 9.5 GHz, although qualitatively similar results are obtained at 9.0 and 10.0 GHz.

The threshold electric and magnetic fields for these "contactless" loop samples were considerably higher than those previously reported.[2-6] There appeared to be no definite correlation between the threshold fields and the two sample orientations that were used.

To test the effects of "contacts" on the microwave emission from loop samples, 3 samples were cut apart and soldered back together as shown in Fig. XII-27. Two

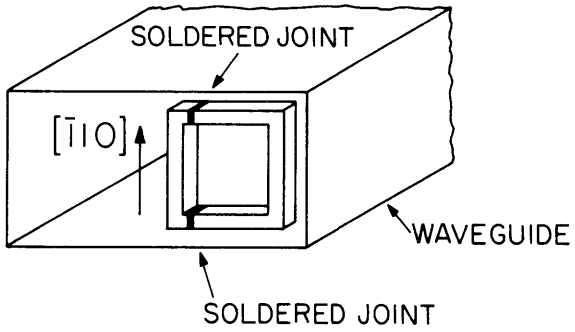

Fig. XII-27. Loop sample with contacts, showing location of contacts and position of the sample in waveguide.

different soldering techniques were employed. In the first, the InSb pieces were joined directly by using pure indium as a solder with a $ZnCl_2$-based flux. In the second method, the InSb surfaces were electroplated with tin, and these plated surfaces were joined by

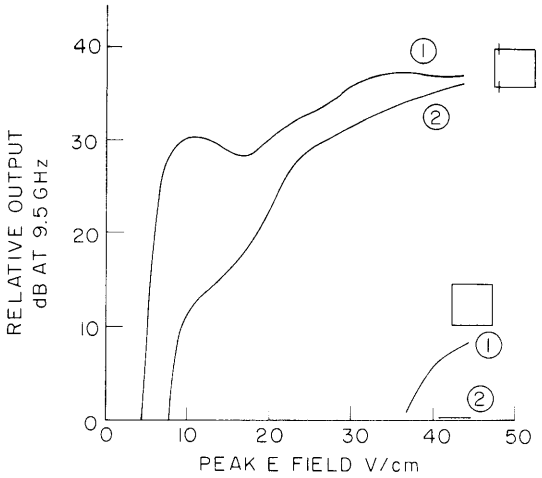

Fig. XII-28.

Direct comparison of microwave emission from samples "1" and "2" before and after contacts were inserted. Frequency of observation: 9.5 GHz. Receiver threshold taken at 0 dB and 40 dB corresponds approximately to 20,000°K equivalent noise temperature. Static magnetic field: 5050 Gauss. 20-MHz RF pulse: 50 pps, 50-μsec duration.

using Wood's metal as a solder. It was not determined directly that the contacts produced in the loop samples were ohmic; however, both soldering techniques have produced ohmic contacts previously. No effects were observed which could be attributed

to the different soldering techniques that were used. Soldered samples were positioned in the waveguide as shown in Fig. XII-27.

Threshold electric and magnetic fields for microwave emission from the 3 soldered samples are indicated in Fig. XII-26. The recorded values agree in a general way with those found by other workers[2-6] who used rod-shaped samples. The general shape of the threshold curve was similar for loop samples with and without contacts. The actual threshold fields for soldered samples were much smaller than those for "intact" samples.

Figure XII-28 shows a direct comparison of two loop samples before and after contacts were inserted. Microwave emission at 9.5 GHz is plotted as a function of peak-induced electric field for constant DC magnetic field. For the two samples shown, contacts increased the microwave emission by roughly 30 dB. Emission from samples without contacts was quite close to the receiver threshold, so details of its behavior were difficult to observe. It appeared, however, to have the same general dependence on electric and magnetic fields as emission from samples with contacts.

Comparison with Previous Work – Conclusions

Following the previous report, we found that the sample for which data were recorded contained some cracks in its surface. A continuous current path through unbroken material existed around the loop, but the cracks provided some local discontinuities. The magnitude of the microwave emission recorded from this sample and the threshold electric and magnetic fields that it required correspond fairly well to the case of the loop samples with contacts in the more recent work. This result and the obvious increase in emission occurring when contacts are inserted in a loop sample suggest that discontinuities in the crystal, such as cracks or contacts, greatly enhance low-field emission from InSb.

The qualitative similarity of the threshold curves for loop samples with and without contacts indicates that the same basic physical process may act in both cases. One might speculate that the emission observed from intact or "contactless" loop samples depends in some way upon naturally occurring discontinuities or imperfections distributed through the crystal. A preliminary theoretical investigation of this last possibility has been started.

R. N. Wallace

References

1. R. N. Wallace, "Low-Field Microwave Emission from Contactless Indium Antimonide Samples," Quarterly Progress Report No. 87, Research Laboratory of Electronics, M.I.T., October 15, 1967, pp. 121-129.
2. S. J. Buchsbaum, A. G. Chynoweth, and W. L. Feldmann, J. Appl. Phys. 37, 2922 (1966).
3. T. Musha, F. Lindvall, and J. Hägglund, Appl. Phys. Letters 8, 157 (1966).
4. J. C. Eidson and G. S. Kino, Appl. Phys. Letters 8, 183 (1966).
5. G. Bekefi, A. Bers, and S. R. J. Brueck, Phys. Rev. Letters 19, 24 (1967).
6. S. J. Buchsbaum, A. G. Chynoweth, and W. L. Feldmann, Appl. Phys. Letters 6, 67 (1965).

2. ACOUSTIC WAVE AMPLIFICATION AT MICROWAVE FREQUENCIES

In pure semiconductors and semimetals microwave acoustic amplification by drifting electrons is dominated by resonant particle-wave interactions. This is a consequence of the fact that at these high frequencies the mean-free path of the electrons becomes comparable to, or greater than, the wavelength of the acoustic wave; that is, $qv_T/\nu \gtrsim 1$, where q is the wave number of the acoustic wave ($q = \omega/v_s$, with v_s the sound phase velocity), v_T is the electron's thermal velocity $\left(v_T^2 = \kappa T/m^*\right.$ the effective mass$\left.\right)$, and ν is the electron's effective collision frequency. Our recent studies[1-3] have revealed the main interaction mechanisms for acoustic-wave amplification in the presence of an applied magnetic field $\overline{B}_o$ along the electron's drift motion. The drift motion of the electrons is established by an external electric field $\overline{E}_o$. In our previous studies we neglected the effect of this electric field upon the interaction. In this report we shall give the result of an analysis that accounts for the presence of the applied electric field, and allows us to estimate its effect upon the interaction.

It has been shown previously[1-4] that the growth rate of the acoustic wave is proportional to the imaginary part of the electrons' dielectric constant. Hence we shall consider the effect of the applied electric field on the electrons' dielectric constant. We first assume a classical description of the electrons, as given by the linearized Boltzmann equation for electrostatic perturbations $e^{-i\omega t}\, e^{i\overline{q}\cdot\overline{r}}$:

$$\omega_c \frac{\partial f_1}{\partial \phi} - i(\omega + i\nu - \overline{q}\cdot\overline{w})\, f_1 - \frac{e\overline{E}_o}{m^*}\cdot\frac{\partial f_1}{\partial \overline{w}} = \frac{en_o}{m^*}\overline{E}_1\cdot\frac{\partial f_o}{\partial \overline{w}} + \nu n_1 f_{OL}, \tag{1}$$

where $\omega_c = eB_o/m^*$ is the electron-cyclotron frequency; ϕ is the polar angle in velocity (w) space in a plane perpendicular to $\overline{B}_o$; $f_1(\overline{r}, \overline{w}, t)$, $f_o(\overline{w})$, and $f_{OL}(\overline{w})$ are, respectively, the perturbed, unperturbed and local distribution functions; n_o and $n_1(\overline{r}, t)$ are, respectively, the unperturbed and perturbed electron densities; and $\overline{E}_1$ is the total first-order electric field, which may include the effective electric field attributable to deformation potential coupling, as well as the self-consistent field (via Poisson's equation) arising from n_1 and the piezoelectric polarization. The solution of Eq. 1, together with Poisson's equation, gives the electrons' longitudinal dielectric constant $K_\ell(\omega, \overline{q})$. We have previously given this solution for the case in which the term containing $\overline{E}_o$ in Eq. 1 was neglected.[1] Now, retaining this term we proceed as follows. Assume that the $\overline{E}_o$ is parallel to $\overline{B}_o$ and gives rise to a drifted Maxwellian distribution for $f_o(w)$, with drift velocity $\overline{v}_D$ parallel to $\overline{B}_o$ and thermal velocity v_T.

$$f_o(w) = \frac{1}{(2\pi)^{3/2} v_T^3} \exp\left[-\frac{(w_{||} - v_D)^2}{2v_T^2}\right] \exp\left(-\frac{w_\perp^2}{2v_T^2}\right). \tag{2}$$

The relaxation is assumed to be to a Maxwellian distribution

$$f_{OL}(w) = f_o(w, v_D = 0). \tag{3}$$

Then, it can be shown[5] that the solution of Eq. 1 for n_1 can be transformed to the solution of the following equations:

$$n_1 = \int f_1 \, d^3w = \int g_1 \, d^3w \tag{4}$$

$$\omega_c \frac{\partial g_1}{\partial \phi} - i(\omega + i\nu - \overline{q} \cdot \overline{w}) \, g_1 = \frac{en_o}{m^*} \overline{E}_1 \cdot \frac{\partial g_o}{\partial \overline{w}} + \nu n_1 g_{OL}, \tag{5}$$

where

$$g_o(w) = \frac{1}{(2\pi)^{3/2} \, v_T^2 v_{T\|}} \exp\left[- \frac{(w_\| - v_D)^2}{2v_{T\|}^2} \right] \exp\left(\frac{-w_\perp^2}{2v_T^2} \right) \tag{6}$$

$$g_{OL}(w) = g_O(w, v_D = 0) \tag{7}$$

and

$$v_{T\|} = v_T \left(1 - i \, \frac{eE_o}{m^* v_T^2 q_\|} \right)^{1/2}. \tag{8}$$

Now we note that Eq. 5 is of the same form as Eq. 1 with $\overline{E}_o = 0$, and hence its solution can be immediately written by using the results of our previous work.[1, 2] The modifications of our previous results come from Eqs. 6-8, which show that the applied electric field parallel to $\overline{B}_o$ has the effect of modifying the electrons' thermal velocity in that direction from v_T to the complex value $v_{T\|}$ given by Eq. 8. From Eq. 8 we note that this modification is only important if the energy gained by an electron in traversing a distance of one wavelength along the field becomes greater than the electrons' thermal energy. Another way of estimating this effect is to note that $v_D = eE_o/m^*\nu$, and therefore

$$\frac{eE_o}{m^* v_T^2 q_\|} = \frac{v_D}{v_T} \frac{\nu}{q_\| v_T}. \tag{9}$$

Hence, for drift velocities that are small compared with thermal velocities and mean-free paths that are long compared with a wavelength along the field, the change in v_T along the field is negligible and our previous results remain essentially unchanged.

We now summarize the detailed results of solving Eqs. 4 and 5 with Poisson's equation for the longitudinal dielectric constant $K_\ell(\omega, \bar{q})$.

Zero Magnetic Field, $\bar{B}_o = 0$; Wave Vector $\bar{q}$ at Any Angle to $\bar{E}_o$

$$K_\ell(\omega, q) = 1 + \frac{\frac{\omega_p^2}{q^2}\int d^3w \, \frac{\bar{q}\cdot(\partial g_o/\partial \bar{w})}{(\omega+i\nu-\bar{q}\cdot\bar{w})}}{1 - i\nu\int d^3w \, \frac{g_{OL}(w)}{(\omega+i\nu-\bar{q}\cdot\bar{w})}}, \tag{10}$$

where $\omega_p^2 = e^2 n_o/m^*\epsilon_L$, and ϵ_L is the lattice dielectric constant.

Using Eqs. 6-8, we obtain

$$K_\ell(\omega, \bar{q}) = 1 + \frac{\omega_p^2}{q^2 v_{TD}^2} \, \frac{1 + \zeta_D Z(\zeta_D)}{1 + \frac{i\nu}{qv_{TD}\sqrt{2}} Z(\zeta)}, \tag{11}$$

where

$$v_{TD} = v_T\left(1 - i\,\frac{e\bar{E}_o\cdot\bar{q}}{m^* v_T^2 q^2}\right)^{1/2} \tag{12}$$

$$\zeta_D = \frac{\omega + i\nu - \bar{q}\cdot\bar{v}_D}{qv_{TD}\sqrt{2}} \tag{13}$$

$$\zeta = \frac{\omega + i\nu}{qv_{TD}\sqrt{2}}, \tag{14}$$

and $Z(\zeta)$ is the plasma dispersion function.[6] These results differ from those of Pines and Schrieffer,[5] in that they did not include a proper relaxation to local equilibrium and therefore have missed the denominator in Eq. 11.

Finite Magnetic Field; $\bar{B}_o$ Parallel to $\bar{E}_o$; q at Any Angle to $\bar{B}_o$ and E_o

$$K_\ell(\omega, \bar{q}) = 1 + \frac{\frac{\omega_p^2}{q^2}\int d^3w \sum_{n=-\infty}^{\infty} J_n^2(p) \, \frac{\frac{n\omega_c}{w_\perp}\frac{\partial g_o}{\partial w_\perp} + q_{||}\frac{\partial g_o}{\partial w_{||}}}{(\omega+i\nu-q_{||}w_{||}-n\omega_c)}}{1 - i\nu\int d^3w \sum_{n=-\infty}^{\infty} \frac{J_n^2(p)\, g_{OL}(w)}{(\omega+i\nu-q_{||}w_{||}-n\omega_c)}}, \tag{15}$$

where $p = q_\perp w_\perp/\omega_c$ and J_n is the ordinary Bessel function of order n. Using Eqs. 6-8, we obtain

$$K_\ell(\omega, \bar{q}) = 1 + \frac{\dfrac{\omega_p^2}{q^2 v_{T\|}^2}\left\{1 + \sum_{n=-\infty}^{\infty} I_n(\lambda)\, e^{-\lambda}\left[\zeta_{DO} - \dfrac{n\omega_c\left(1 - v_{T\|}^2/v_T^2\right)^{1/2}}{q_\| v_{T\|}\sqrt{2}}\right] Z(\zeta_{Dn})\right\}}{1 + \dfrac{i\nu}{q_\| v_{T\|}\sqrt{2}} \sum_{n=-\infty}^{\infty} I_n(\lambda)\, e^{-\lambda}\, Z(\zeta_n)} \tag{16}$$

where

$$\zeta_{Dn} = \frac{\omega + i\nu - q_\| v_D - n\omega_c}{q_\| v_{T\|}\sqrt{2}} \tag{17}$$

$$\zeta_n = \frac{\omega + i\nu - n\omega_c}{q_\| v_{T\|}\sqrt{2}} \tag{18}$$

$$\lambda = \left(\frac{q_\perp v_T}{\omega_c}\right)^2. \tag{19}$$

I_n is the modified Bessel function, and Z is the plasma dispersion function.[6] For $v_{T\|} = v_T$ these reduce to our previous results.[1,2]

Finally we discuss quantum-mechanical effects. We have already given a complete quantum-mechanical derivation for $K_\ell(\omega, \bar{q})$,[1] and from the present results its modification to include the effects of $\bar{E}_o$ is obvious. The changes in the interaction caused by quantum mechanical effects can be separated as follows. First, for large magnetic fields such that $\omega_c \gg \nu$ and $\hbar\omega_c \gg \kappa T$ the electron distribution function must be explicitly modified to exhibit the Landau levels. Second, for large wave numbers such that $(\hbar q/m^*) > v_D$ or v_T all of the energy resonances must be modified to include the effects of recoil in particle-wave interactions. Thus $\omega + i\nu - q_\| v_D - nw_c \rightarrow \omega + i\nu - q_\| v_D - n\omega_c - \hbar q^2/2m^*$ in all terms containing ζ or ζ_D. For acoustic waves ($q = \omega/v_s$) these recoil effects may become important at high microwave frequencies. Further studies along these lines continue.

A. Bers, S. R. J. Brueck

References

1. A. Bers and T. Musha, Quarterly Progress Report No. 79, Research Laboratory of Electronics, M.I.T., October 15, 1965, pp. 94-109.

2. S. R. J. Brueck and A. Bers, Quarterly Progress Report No. 83, Research Laboratory of Electronics, M.I.T., October 15, 1966, pp. 72-76.

3. S. R. J. Brueck, S.M. Thesis, Department of Electrical Engineering, M.I.T., February 1967.

4. A. Bers, Quarterly Progress Report No. 88, Research Laboratory of Electronics, M.I.T., January 15, 1968, pp. 204-209.

5. In the absence of an applied magnetic field this was first given by D. Pines and J. R. Schrieffer, Phys. Rev. 124, 1387-1400 (1961). The generalization of their results to the case when an applied magnetic field is present was suggested to us by A. L. McWhorter (unpublished).

6. B. Fried and S. Conte, The Plasma Dispersion Relation (Academic Press, Inc., New York, 1961).

3. COLLISIONAL EFFECTS ON ACOUSTIC-WAVE AMPLIFICATION AT MICROWAVE FREQUENCIES

We have previously reported on the problem of the amplification of acoustic waves by drifting electrons in a semiconductor.[1] In this report we give some results obtained by using a more realistic collision model. This study was motivated by an analysis of Blötekjaer,[2] in which he used a transport-model formulation of the problem along with a collision model similar to that presented here. He found a saturation of the gain at high frequencies $\left(\omega \sim \nu \frac{v_s^2}{v_T^2}\right.$; with ν the collision frequency, v_s the acoustic-wave phase velocity, and v_T the electron thermal velocity$\left.\right)$. We have considered the case of long mean-free path ($q\ell \gg 1$; with q the wave vector, and ℓ the mean-free path) and have therefore used the Boltzmann equation. As we found previously,[1] the major part of the gain in this case arises from resonant wave-particle interactions, and collisions are found to modify the results only slightly. In this report we show this explicitly for an electron-collision model which accounts for both energy and momentum relaxation.

The electron system is described by the Boltzmann equation

$$\frac{\partial f}{\partial t} + \bar{w} \cdot \frac{\partial f}{\partial \bar{r}} + \frac{\bar{F}}{m} \cdot \frac{\partial f}{\partial \bar{w}} = \left(\frac{\partial f}{\partial t}\right)_{coll}, \tag{1}$$

where $\bar{w}$ is the velocity variable in phase space, $n_o f(\bar{r}, \bar{w}, t)\, d^3r d^3w$ is the density of particles at time t within the differential volume $d^3r d^3w$ around $(\bar{r}, \bar{w})$, n_o is the average density, $\bar{F}$ is the force on a particle, and m is the electron mass. As a result of the slow-wave phase velocities that are of interest, the quasi-static approximation can be shown to be valid[1]; therefore, $\bar{F} = -e\bar{E}$ (e is the electron charge magnitude), and Eq. 1 must be solved self-consistently with Poisson's equation.

$$\epsilon_L \nabla \cdot \bar{E} = -en(\bar{r}, t), \tag{2}$$

where $n(\bar{r}, t) = \int n_o f(\bar{r}, \bar{w}, t)\, d^3w$, and ϵ_L is the background dielectric constant of the lattice.

The collision term is taken as

$$\left(\frac{\partial f}{\partial t}\right)_{coll} = -\nu \left[f(\bar{r}, \bar{w}) - \frac{n/n_o}{(2\pi)^{3/2} (\overline{w^2})^{3/2}} \exp(-w^2/2\overline{w^2}) \right]$$

$$- \nu_e \left[f(\bar{r}, \bar{w}) - \frac{n/n_o}{(2\pi)^{3/2} v_T^3} \exp\left(-w^2/2v_T^2\right) \right], \tag{3}$$

where $\overline{nw^2} = \frac{n_o}{3}\int \left(w_x^2+w_y^2+w_z^2\right) f\, d^3w$, and $v_T^2 = \frac{\kappa T}{m}$ is the thermal velocity (κT, the temperature in energy units). The properties of this collision term are best understood by taking the first three moment equations of the Boltzmann equation:

$$(0)\quad \frac{\partial n}{\partial t} + \frac{\partial}{\partial x_i}(nv_i) = 0 \tag{4a}$$

$$(1)\quad \frac{\partial v_i}{\partial t} + v_j \frac{\partial}{\partial x_j} v_i + \frac{1}{n}\frac{\partial}{\partial x_j}(n\overline{u_i u_j}) + \frac{eE_i}{m} = -(\nu+\nu_e)v_i \tag{4b}$$

$$(2)\quad nv_j \frac{\partial v_i}{\partial t} + \frac{\partial}{\partial t}(n\overline{u_i u_j}) + nv_j v_k \frac{\partial}{\partial x_k} v_i + \frac{\partial}{\partial x_k}\left[n(v_j\overline{u_i u_k}+v_k\overline{u_i u_j}+\overline{u_i u_j u_k}\right] + \frac{eE_i}{m} v_j n$$

$$= -\nu n\left(\overline{u_i u_j} - \overline{w^2}\delta_{ij}\right) - \nu_e n\left(u_i u_j - v_T^2 \delta_{ij}\right). \tag{4c}$$

In Eqs. 4 $v_i = \overline{w}_i$, $u_i = w_i - v_i$, and the bars denote averaging over the distribution function; for example, $\overline{a} = \int a n_o f\, d^3w$, and the summation convention has been used throughout.

Inspection of these equations indicates that the first collision term in Eq. 3 relaxes momentum about zero and, while not involving any energy loss from the electron system, relaxes velocity space anisotropies in the distribution function. The second term relaxes momentum around zero, and also relaxes energy isotropically to the lattice thermal energy. Physically, then, the first term represents an elastic scattering process in which momentum is completely randomized, and consequently any organized particle energy is converted into random thermal energy. The second term represents an inelastic scattering process in which the momentum is again randomized, and sufficient energy is also removed from the electrons to bring them into thermal equilibrium with the lattice. If acoustic phonon scattering is the dominant relaxation mechanism for both energy and momentum, then the collision frequencies are related by[2]

$$\nu + \nu_e = \frac{v_T^2}{v_s^2}\nu_e. \tag{5}$$

This model was chosen simply to give the correct moment equations and it is clear that it cannot adequately account for actual collision processes in solids; therefore, we shall take (4) only as giving a general idea of the relative orders of magnitude of ν and ν_e.

Equations 1-3 can be solved by the usual linearization and Fourier-Laplace transform techniques. The dielectric constant for the electrons is found to be

$$K_\ell(\omega,\bar{q}) = 1 - \frac{\dfrac{\omega_p^2}{2q^2v_T^2}\left[Z'(\zeta_D) - \dfrac{i\nu}{3qv_T}A\right]}{1 - \dfrac{i(\nu+\nu_e)}{qv_T}B}, \tag{6}$$

where

$$\zeta_D = \frac{\omega + i\nu - q_{\|}v_D}{qv_T\sqrt{2}},$$

with v_D the electron's drift velocity, $\omega_p^2 = e^2n_o/m^*\epsilon_L$ the plasma frequency, and Z' the derivative of the plasma dispersion function,[3] and A and B are complicated functions of order one. The growth rate of an acoustic wave interacting with the electrons is proportional to Im $[K_\ell(\omega,\bar{q})]$. For microwave frequencies, and relatively pure semiconductors, $(\nu/qv_T) \sim 0.01$, and hence the main contribution to $K_\ell(\omega,\bar{q})$ comes from the first term in the numerator of Eq. 6. Expanding $K_\ell(\omega,\bar{q})$ to first order in ν/qv_T and ω/qv_T, we obtain

$$K_\ell(\omega,\bar{q}) \approx 1 - \frac{\omega_p^2}{2q^2}\left[\frac{Z'(\zeta_D)}{v_T^2}\left(1 + \frac{3}{2}\frac{\nu}{qv_o}\sqrt{\frac{\pi}{2}} + \frac{\nu_e}{qv_T}\sqrt{\frac{\pi}{2}}\right)\right.$$
$$\left. + \frac{\nu}{qv_o^3}\sqrt{\frac{\pi}{2}}\left(-\frac{1}{3} + Z'(\zeta_D)\left(1 + \frac{v_D^2\sin^2\theta}{2v_T^2}\right)\right)\right], \tag{7}$$

where $v_o^2 = v_T^2 + v_D^2/3$.

In conclusion, we find that at microwave frequencies with $(\nu/qv_T) \ll 1$, the electron dielectric constant, and hence the acoustic wave amplification, is dominated by resonant wave-particle interactions, and collisions play a minor role. The results of Blötekjaer[2] are only valid for lower frequencies with $(\nu/qv_T) \gg 1$.

S. R. J. Brueck, A. Bers

References

1. S. R. J. Brueck and A. Bers, Quarterly Progress Report No. 83, Research Laboratory of Electronics, M.I.T., October 15, 1966, pp. 72-76, and S. R. J. Brueck, S. M. Thesis, M.I.T., February 1967 (unpublished).
2. K. Blötekjaer, Ericsson Technics No. 2 (1966), p. 125. See also Proc. IEEE 55, 432 (1967).
3. B. Fried and S. Conte, The Plasma Dispersion Relation (Academic Press, Inc., New York, 1961).

4. ACOUSTIC WAVE AMPLIFICATION-TRANSPORT THEORY

In a previous report,[1] a simple formulation of acoustic wave interactions with drifting electrons in a magnetic field was derived. The simplicity of a transport-theory model (assuming $\nu \gg \omega$ and $\nu \gg qw$) for the electrons allowed us to explore a variety of geometrical arrangements for the applied electric and magnetic fields. The frequency of maximum acoustic growth was found to depend only upon the material parameters, and

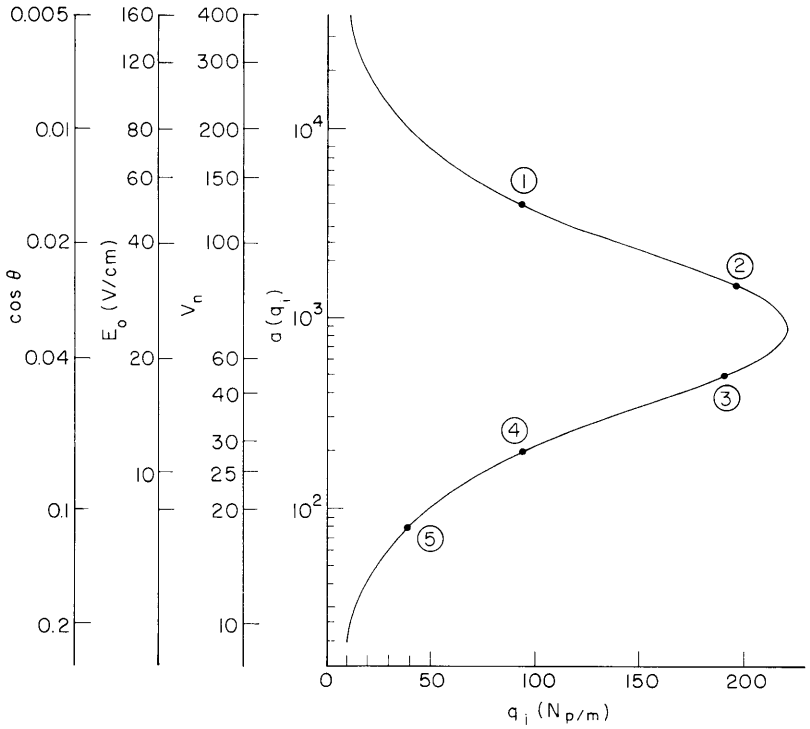

Fig. XII-29. The gain parameter $a(q_i)$ vs q_i (Eq. 6). The other vertical scales refer to configuration (a) and InSb parameters,[1] when v_n for $b \to \infty$ is minimized with respect to cos θ.

the maximum growth rate at this frequency was studied as a function of drift velocity, applied magnetic field, and direction of acoustic wave propagation. In several instances we found that this maximum growth of the acoustic wave occurred only for high applied electric fields that would violate the assumptions of the simple transport-theory model. (For the example of InSb, $v_n = 100$ corresponded to a drift velocity equal to the electrons' thermal velocity.)

In this report we shall describe the applied field characteristics of lower growth rates at the frequency of maximum gain. Our starting point is the gain equation, Eq. 13,

from the previous report[1] which is reproduced here at the frequency of maximum gain (Eq. 15)[1]:

$$q_i = \frac{P^2}{2}\frac{\omega_o}{v_s}\frac{b_\ell \delta}{\delta^2 + 4b_\ell^2 \frac{\omega_o}{\omega_D}}. \tag{1}$$

For the three configurations (Fig. XXIII-32)[1] in the previous report we have (Eq. 14)[1]:

Configuration (a) $\delta = v_n \cos\theta - 1$ (2)

(b) $\delta = v_n \sin\theta - 1$ (3)

(c) $\delta = v_n \frac{b}{1+b^2} \sin\theta - 1.$ (4)

We now solve Eq. 1 for δ and write it as follows

$$\delta = b_\ell a(q_i), \tag{5}$$

where

$$a(q_i) = \frac{1}{q_i}\left[\frac{P^2\omega_o}{4v_s} \pm \sqrt{\frac{P^4\omega_o^2}{16v_s^2} - 4q_i^2\frac{\omega_o}{\omega_D}}\right]. \tag{6}$$

The material parameters and gain are all combined in $a(q_i)$. We have plotted $a(q_i)$ in Fig. XII-29. In order to get some idea of how $a(q_i)$ is related to parameters of interest, we have evaluated these for the particular example of InSb (see Bers[1]), and they are shown on the three vertical scales of Fig. XII-29. These were obtained as follows. First, we substituted in Eq. 1 the parameters for configuration (a). Then we let $b \to \infty$, which appeared to minimize v_n (with respect to b). We then minimized v_n with respect to $\cos\theta$. These values of $\cos\theta$ comprise one scale in Fig. XII-29, and the corresponding v_n values are given on another scale. This scale for v_n and the material parameters then yield the corresponding minimum values of applied electric field, E_o, which are also shown. This gives an interpretation for the values of $a(q_i)$. It is single-valued only at the maximum q_i; at all other places the gain can be reduced by either a too high or too low drift velocity.

From here we proceed to pick some points on Fig. XII-29 (1-5) and plot graphs of normalized drift velocity against magnetic field for several values of propagation angle, in all three configurations. Figure XII-30 presents a matrix of these graphs. The graphs corresponding to maximum q_i (20 dB/cm gain) were given in the previous report.

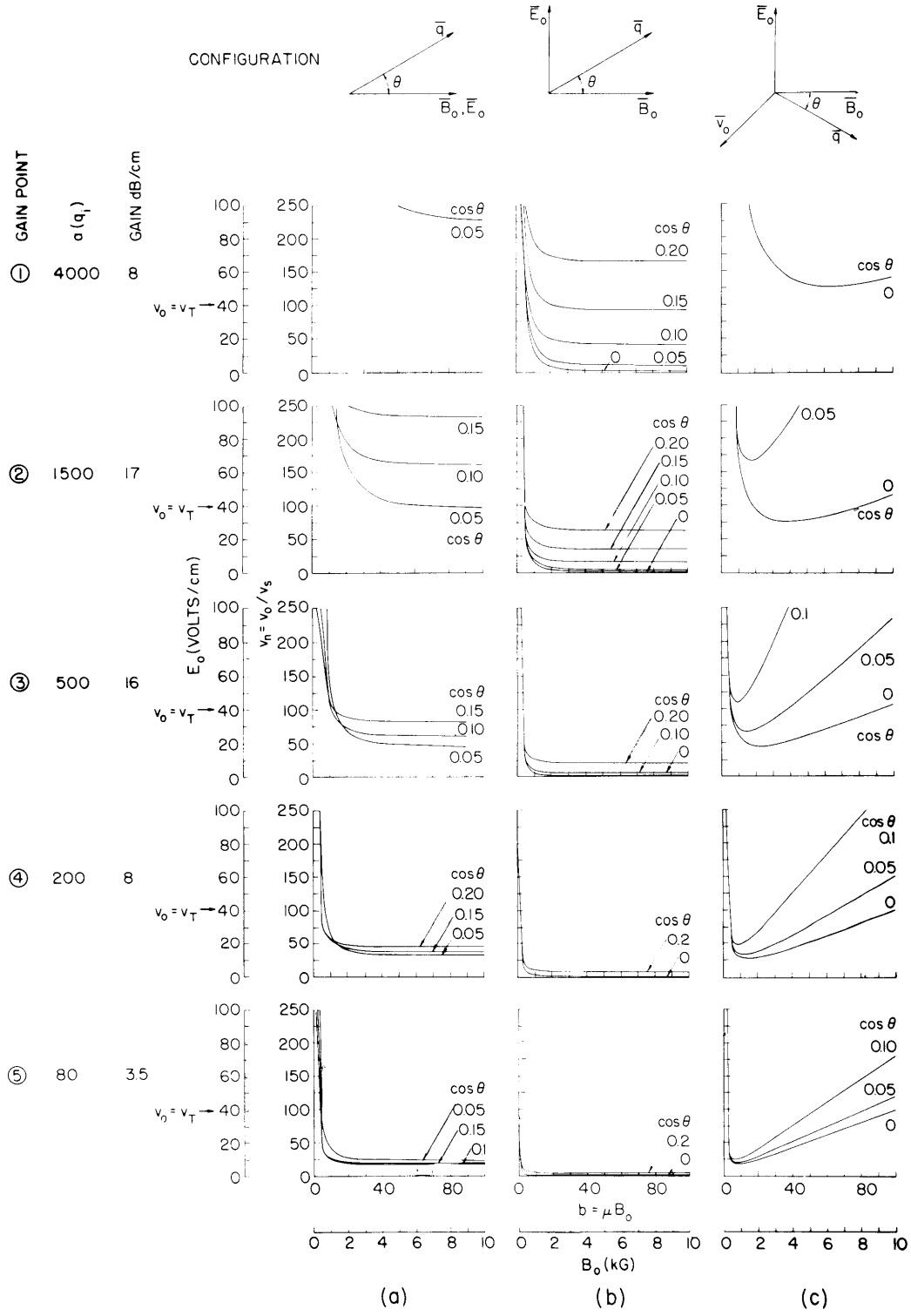

Fig. XII-30. Normalized drift velocity vs normalized magnetic field at the frequency of greatest gain. The electric and magnetic fields are calculated for InSb at 77°K as in the previous report.[1]

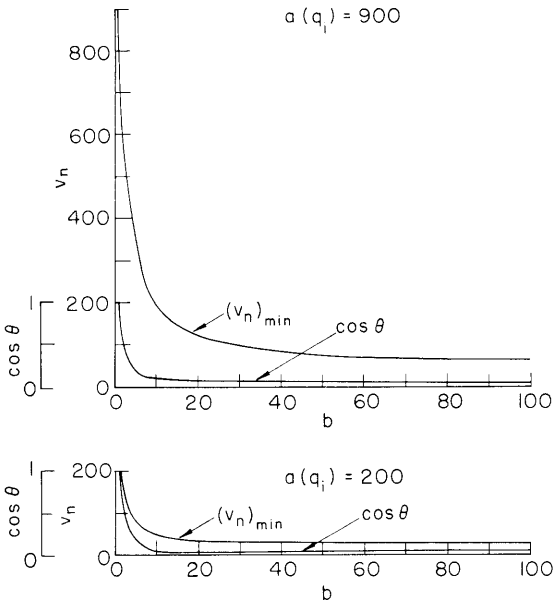

Fig. XII-31. Minimum drift velocity and propagation angle vs magnetic field for configuration (a), at maximum gain (a = 900) and for a = 200.

For configuration (a) we note that for a given gain and magnetic field the minimum drift velocity (v_o) and propagation direction (θ) are given by

$$\cos\theta = \begin{cases} \dfrac{1 + b^2 + a}{ab^2} & \text{for} \quad b > \dfrac{a+1}{a-1} \\ 1 & \text{for} \quad b < \dfrac{a+1}{a-1} \end{cases} \tag{8}$$

$$(v_n)_{min} = \begin{cases} \dfrac{2b}{1+b^2} & \text{for} \quad b > \dfrac{a+1}{a-1} \\ a + 1 & \text{for} \quad b < \dfrac{a+1}{a-1}. \end{cases} \tag{9}$$

Figure XII-31 shows Eqs. 8 and 9 plotted against b for two values of $a(q_i)$ corresponding to the maximum gain condition and a lower gain (point 4 in Fig. XII-29).

Further theoretical work and computations are in progress.

D. A. Platts, A. Bers

References

1. A. Bers, Quarterly Progress Report No. 88, Research Laboratory of Electronics, M. I. T., January 15, 1968, pp. 204-209.

5. CRITERIA FOR NEGATIVE-ENERGY HELICON WAVES

Passive helicon waves have been studied by many workers in the past in several different materials.[1-3] By drifting the electrons, it is possible to create a negative-energy helicon wave that may then be coupled to a suitable system to create growth. Calculations by Bers and McWhorter[4] for the case of an infinite medium show that an infinitesimal carrier drift will produce a negative-energy wave. For a bounded plasma, however, there is a definite lower threshold for the electron drift. The problem of a passive helicon in a cylindrical plasma has been worked out by Klozenberg, McNamara, and Thonemann[5] (KMT). Using these calculations and imposing an electron drift, we examine the criteria for negative-energy helicons in indium antimonide and lead telluride with cylindrical boundaries. We conclude that for crystals of reasonable size, a negative-energy mode is unlikely to be found in indium antimonide, and there are marginal chances of finding such a mode in lead telluride.

KMT have computed the dispersion characteristics of undrifted helicons for several of the lowest modes (m) of the bounded plasma. We examined the m = 0 mode because it has the lowest threshold drift velocity.

There are several specific criteria to be met in a material.

(i) To drift electrons sufficiently fast, a large DC current pulse must be applied to the sample. The crystal can only dissipate a certain amount of energy that it acquires in the form of heat from the current. To prevent overheating of the crystal, the drift current must be pulsed. To establish a periodic helicon wave, the period T must be short compared with the pulse length τ_c.

(ii) Large damping of the helicon wave will exist unless the imaginary part of the wave vector k_i is small compared with the real part of the wave vector k_r. We require that the ratio $\xi = k_i/k_r$ be small and favor values of $\xi \sim 0.1$.

(iii) The sample must be at least a few wavelengths of the helicon wave, and we favor a length $\ell \sim 4\lambda$.

(iv) To reduce the damping on the negative-energy helicon wave, $\omega_c\tau$ should be as large as possible, where ω_c is the electron-cyclotron frequency, and τ is the time between collisions. Since $\omega_c\tau = \mu B$, we want a high value of μB. We favor $\mu B \sim 30$.

Symbols used in this note (in MKS system) are the following.

n, electron density

e, electron charge

μ, electron mobility

μ_o, permeability of free space

a, sample radius

B, magnetic field

E, electric field.

To facilitate our study, we shall try to use dimensionless quantities whenever possible:

$$\omega/\omega_o = \left[\frac{(\mu B)}{ne\mu\mu_o a^2}\right]^{-1} \omega$$

$(\mu B) = \omega_c \tau$, where ω_c is the electron-cyclotron frequency, and τ is the collision frequency.

ak_r, a measure of the radial dimension of the plasma in units of wavelength.

$s = \frac{\omega/\omega_o}{ak_r}$, the slope of the helicon dispersion curve in dimensionless terms near the origin, $\omega = k_r = 0$.

α, the ratio of current pulse time τ_c to wave period T.

$\xi = k_i/k_r$.

The m = 0 mode of a bounded plasma as calculated by KMT is shown in Fig. XII-32, together with the helicon mode for an infinite medium. A line with slope $s = \frac{\omega/\omega_o}{ak_r} = 3.3$ has been added to the figure. The slope of 3.3 barely exceeds the slope of the tangent line to the KMT dispersion curve at the origin $\omega = k_r = 0$, and thus represents the smallest drift velocity required for a negative-energy wave. This drift velocity is related to s by

$$v_d = a\omega_o s$$

$$v_d = \frac{(\mu B)s}{ne\mu\mu_o a}. \tag{1}$$

The current density J required to produce a negative-energy wave is, therefore,

$$J = nev_d$$

or from Eq. 1,

$$J = \frac{(\mu B)s}{\mu\mu_o a} \tag{2}$$

We thus obtain a relation for the power requirements

$$P = IV = IE\ell = \frac{I^2\ell}{ne\mu\pi a^2}.$$

Using $I = J\pi a^2$ and Eq. 2, we obtain

$$P(\text{watts}) = \frac{\pi a s^2 (\mu B)^2 (\ell/a)}{ne\mu^3 \mu_o^2}. \tag{3}$$

Also,

$$V(\text{volts}) = E\ell = \frac{(\mu B)\, s(\ell/a)}{ne\mu^2 \mu_o}. \tag{4}$$

It is important to note that Eq. 4 for the voltage is independent of the size of the sample. The shape does enter through ℓ/a, which we shall see is a function of material. Since we know the maximum electric field that can be established on a material without

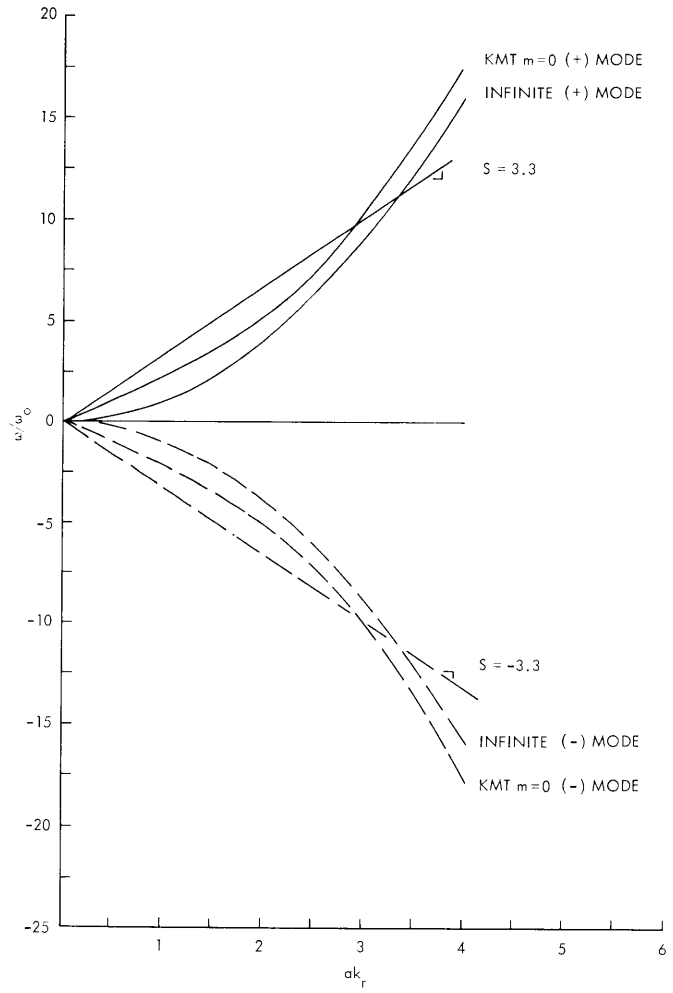

Fig. XII-32. Dispersion relation for traveling waves.

causing avalanche or runaway (as the case may be), we expect to be able to use $V = E_{max}\ell_{min}$ to find a minimum cutoff length for the crystal.

The DC current applied to the sample to cause drifted electrons will also cause the sample to heat. We shall assume conservatively that during the short current pulse none of the energy is dissipated by the ambient coolant (liquid nitrogen or liquid helium). Thus we have $Q = mc_p\Delta T$, where ΔT is the temperature rise of the sample. Because better data were not available, we used the specific heat for silicon as representative of both materials under consideration. If

$$Q = \rho(\pi a^2 \ell)\, c_p \Delta T,$$

where $\rho = 2.4 \times 10^3$ kgm m^{-3} for silicon

$$c_p = 150 \text{ joule kgm}^{-1} \text{ deg}^{-1},$$

then

$$Q(\text{joule}) = 3.65 \times 10^5\, \pi a^2 \ell \Delta T. \tag{5}$$

The pulse time τ_c must be large compared with the period T of the helicon wave. Let us denote the ratio of these two quantities (τ_c/T) by α, for which we shall assume that α is 10 or more. If ω_{min} is the minimum helicon radial frequency and τ_c the pulse time,

$$\omega_{min} = \frac{2\pi\alpha}{\tau_c} = \frac{2\pi\alpha P}{Q}.$$

From Eqs. 3 and 4,

$$\frac{\omega_{min}}{\omega_o} = \frac{2\pi\alpha(\mu B)\, s^2}{3.65 \times 10^5 \mu^2 \mu_o \Delta T}. \tag{6}$$

This establishes a maximum ak_r on the drafted dispersion curve (Fig. XII-35, curve B). It will be shown that we want a small ω_{min} which means we want a large ΔT. But a large rise in the temperature will reduce the electron mobility. Also since we have neglected any heat dissipation mechanisms, we shall permit a fairly large value for the heat rise $\Delta T = 10\text{-}22.5°K$.

The damping of the helicon wave depends on k_i, the imaginary part of the wave vector, through ξ, where $\xi = \frac{k_i}{k_r} = \frac{ak_i}{ak_r}$. We favor values of $\xi \leq 0.1$. Since ak_i is in the region of interest that is not very dependent on ω/ω_o (Fig. XII-33), a lower cutoff is established on the usable range of ak_r, $(ak_r)_{min} = \frac{ak_i}{\xi}$. We therefore can only use values of ak_r for

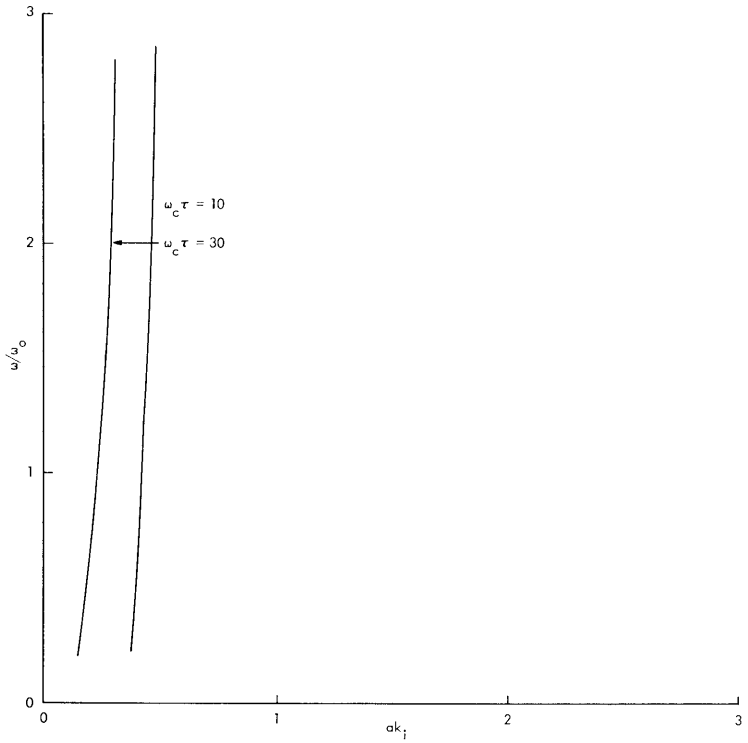

Fig. XII-33. Attenuation constants for drifted traveling waves with m = 0 and two values of $\omega_c\tau$.

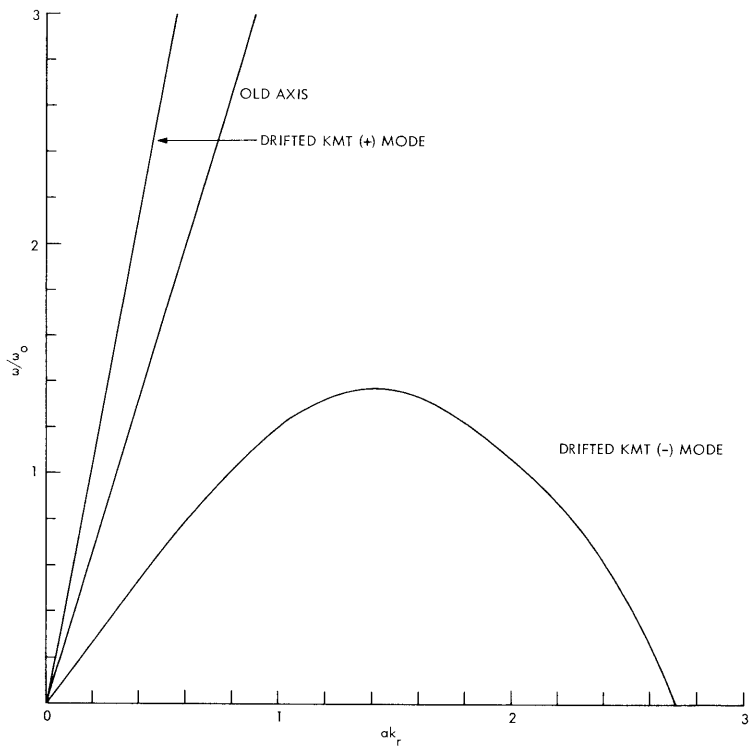

Fig. XII-34. Drifted dispersion relation for finite geometries.

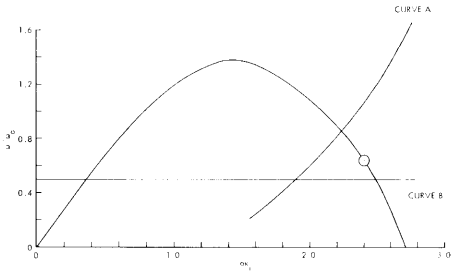

Fig. XII-35

Experimental window. Curve A: Lower limit on ak_r. Curve B: Lower limit on ω/ω_o. The point on the dispersion curve represents desired experimental conditions.

which the damping is at acceptable levels. These values of ak_r appear in Fig. XII-35 at the right of curve A which is $(ak_r)_{min}$.

We have seen how the power (Eq. 3) and the heat (Eq. 5) establish a minimum frequency $\frac{\omega_{min}}{\omega_o}$ that is dependent on material mobility and heat rise through Eq. 6. Therefore we can only use values of ω/ω_o above ω_{min}/ω_o, which restricts us to values above line B in Fig. XII-35.

Lines A and B then map a small window on the dispersion curve where the experiment can be conducted. Now we must see if points exist on the drifted dispersion curve above and at the right of the intersection of curve A and curve B for crystals of reasonable size.

For indium antimonide with a mobility of 50 $m^2\ volt^{-1}\ sec^{-1}$, electron density $n = 10^{20}\ m^{-3}$ and $\mu B = 30$, $\alpha = 10$, $s = 3.3$, from Eq. 6 we find

$$\frac{\omega_{min}}{\omega_o} = \frac{18°K}{\Delta T}. \tag{7}$$

We know from the dispersion curve of Fig. XII-35 that ω_{min}/ω_o must be less than 0.8 at the absolute maximum to open a window in which to conduct an experiment. We see from Eq. 7, however, that ΔT must be 22.5°K to have $\omega_{min}/\omega_o = 0.8$, which still gives almost no window at all with $\xi = 0.1$.

If we do allow a rise of 22.5°K, a small window in Fig. XII-35 at $ak_r = 2.25$, $\omega/\omega_o \sim 0.85$.

$$ak_r = \frac{8\pi a}{\lambda} = \frac{8\pi a}{\ell} = 2.25$$

$$\frac{\ell}{a} = 11.$$

This value of ℓ/a is substituted in Eq. 4 to find $E\ell$. Preliminary experiments indicate that the maximum drift current for indium antimonide is around $10^5\ msec^{-1}$. Since $E_{max} = v_{d_{max}}/\mu$, we find that the maximum allowable electric field is 2×10^3 volts m^{-1}. Since $\ell_{min} = V/E_{max}$,

$$\ell_{min}(meters) = \frac{2.2 \times 10^4}{2 \times 10^3}$$

$$\ell_{min}(meters) = 11.$$

Since this is the minimum length allowed, we eliminate indium antimonide from further consideration, because of the size of the required crystal.

For lead telluride with a mobility of 100 m^2 $volt^{-1}$ sec^{-1}, electron density $n = 10^{23}$ m^{-3} and $\mu B = 30$, $\alpha = 10$, $s = 3.3$, from Eq. 6 we find

$$\frac{\omega_{min}}{\omega_o} = \frac{4.5°K}{\Delta T}. \tag{8}$$

We know from the dispersion curve of Fig. XII-35 that ω_{min}/ω_o must be less than 0.8 to open a window with $\xi = 0.1$. We selected a rather large value of $\Delta T = 10°K$ to compensate for heat dissipation which we were forced to ignore until now. The window then is from $2.25 < ak_r < 2.5$. We can find the ratio of ℓ/a for a value of ak_r in the mid-range of this window. For $\omega/\omega_o = 0.64$, $ak_r = 2.4$, $\ell/a = 10.5$. The voltage across the sample is then given by Eq. 4 to be

$$V = E\ell = 5 \text{ volts}. \tag{9}$$

If we allow a maximum drift velocity of 10^5 m/sec, the maximum electric field is

Table XII-1. Comparison of parameters for lead telluride and indium antimonide.

Parameter	PbTe	InSb
s	3.3	3.3
α	10	10
ξ	0.1	0.1
μB	30	30
$n\,m^{-3}$	10^{23}	10^{20}
$\mu\,m^2$/Volt-sec	100	50
ℓ/a	10.5	11
V volt	5	2.2×10^4
E_{max} Volt/meter	10^3	2×10^3
ℓ_{min} meter	5×10^3	11
a_{min} meter	5×10^{-4}	1
ω_o rad/sec	60×10^6	
$f_o = \omega_o/2\pi$ Hz	9.6×10^6	
f Hz	6.1×10^6	
λ Hz	1.2×10^{-3}	
I_{min} Amps	1250	

10^3 volts meter^{-1}, and the minimum length of the sample is 5 mm. The minimum radius a is 0.5 mm. The other parameters for lead telluride are compared with the corresponding ones for indium antimonide in Table XII-1.

We therefore conclude that a negative-energy wave is very unlikely in indium antimonide. It appears that favorable conditions for a negative-energy wave can be found for lead telluride.

J. H. Spencer

References

1. R. Bowers, C. Legendy, and F. Rose, Phys. Rev. Letters 7, 339 (1961).
2. C. Nanney, Phys. Rev. 138, A1484 (1965).
3. W. Schilz, Phys. Rev. Letters 20, 104 (1968).
4. A. Bers and A. L. McWhorter, Phys. Rev. Letters 15, 755 (1965).
5. J. P. Klozenberg, B. McNamara, and P. C. Thonemann, J. Fluid Mech. 21, (3), 545 (1965).